Clean Technologies and Environmental Policy (2023) 25:2727–2746
https://doi.org/10.1007/s10098-023-02525-z

ORIGINAL PAPER

Physico-chemical characterization of walnut shell biochar from uncontrolled pyrolysis in a garden oven and surface modification by ex-situ chemical magnetization

Rahul Ramesh Nair[1] · Andreas Schaate[2,3] · Lars Frederik Klepzig[4,5] · Ariel E. Turcios[6] · Jacek Lecinski[7] · Madina Shamsuyeva[7] · Hans-Josef Endres[7] · Jutta Papenbrock[6] · Peter Behrens[2,5] · Dirk Weichgrebe[1]

Received: 26 July 2022 / Accepted: 4 April 2023 / Published online: 18 April 2023

Abstract

The shells of walnuts (WS) are major refuse in the global fruits and nuts trade. This, otherwise discarded, lignin-rich material can be carbonized to biochar—a value-added product with environmental applications such as carbon sequestration, soil amelioration, and pollutant adsorption. These applications are dictated by structural and chemical characteristics of the biochar carbon. Conventional controlled pyrolysis (CPy) of biomass is cost-intensive and technically too complex for widespread adoption, especially in emerging economies. Here, walnut shell biochar (BWS0) is derived through uncontrolled pyrolysis (UCPy) in a pyrolysis oven and further hybridized as magnetic biochar through ex-situ chemical co-precipitation. The physico-chemical characteristics of biochar and its water-extractable fractions are comprehensively investigated to understand their carbon structure and environmental applicability. The sp^2 amorphous carbon sequestered in BWS0 is 0.84 $kg_{CO2}/kg_{biomass}$ with a BET (N_2) surface area of 292 m^2/g and is comparable to biochar from CPy in terms of carbon structure. The polyaromatic hydrocarbons present are only trace amounts of naphthalene, biphenyl, and phenanthrene. The magnetization decreases porosity of BWS0 while greatly facilitating its separation from aqueous media. BWS0 is suitable for adsorption of cations (between pH 2.8 and 9.45) and hydrophobic pollutants with only 19 mg L^{-1} fouling from their intrinsic dissolved organic carbon. In combination with fast-release N, P fertilizers, BWS0 (C/N of 24.8) is suitable for application in hydrophilic soils at higher loading rates. The results suggest an avenue where WS biochar can also be prepared via UCPy for direct environmental applications. Future investigations into soil incubation and adsorption tests are recommended.

✉ Rahul Ramesh Nair
nair@isah.uni-hannover.de; rahulgenesis@hotmail.com

[1] Institute of Sanitary Engineering and Waste Management (ISAH), Leibniz University of Hannover (LUH), Hanover, Germany

[2] Institute of Inorganic Chemistry (ACI), LUH, Hanover, Germany

[3] Laboratory of Nano and Quantum Engineering, LUH, Hanover, Germany

[4] Institute of Physical Chemistry and Electrochemistry (PCI), LUH, Hanover, Germany

[5] Cluster of Excellence PhoenixD (Photonics, Optics, and Engineering – Innovation Across Disciplines), LUH, Hanover, Germany

[6] Institute of Botany (IfB), LUH, Hanover, Germany

[7] Institute of Plastics and Circular Economy (IKK), LUH, Hanover, Germany

Graphical abstract

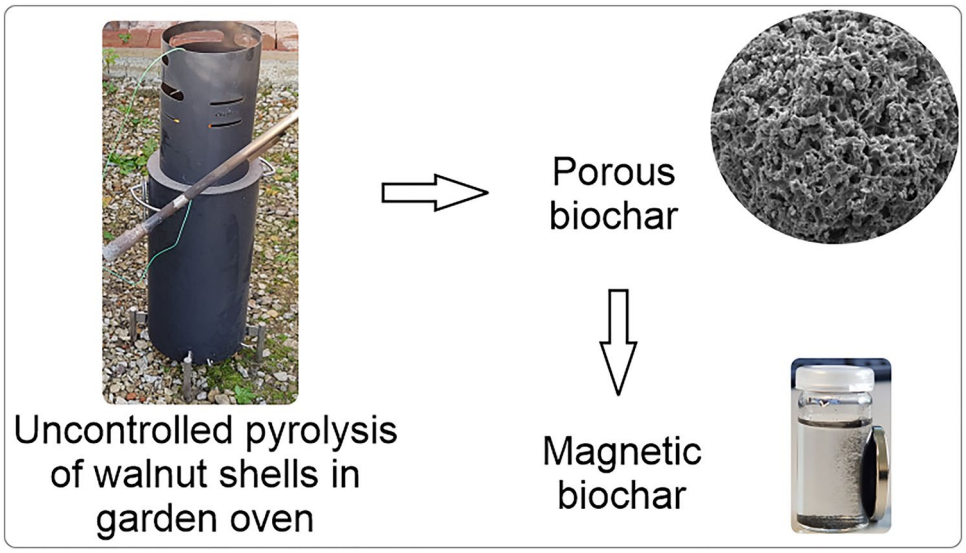

Keywords Uncontrolled pyrolysis · Walnut shell biochar · Chemical co-precipitation · Magnetic biochar · Carbon sequestration

Abbreviations

AAEM	Alkali and alkaline earth metals
AC	Ash content
ATR-FTIR	Attenuated total reflection—Fourier transformed infrared spectroscopy
BET	Brunauer–Emmett–Teller analysis
BWS0	Biochar made from WS
BWS1,2,3	Magnetized BWS0 at decreasing levels of iron content
BWS_{CP}	Pristine biochars from WS produced through controlled pyrolysis
CoP	Chemical co-precipitation
CPy	Conventional controlled pyrolysis
DOC	Dissolved organic carbon
EC	Electrical conductivity
FC	Fixed carbon
HTT	Highest treatment temperature
M_s	Saturation magnetization
MWB	Mineral and ash-rich waste biomass
OFG	Oxygenated functional group
PAH	Polyaromatic hydrocarbons
pH_{pzc}	Point of zero charge
Py-GC–MS	Pyrolysis–gas chromatography-mass spectroscopy
SEM	Scanning Electron Microscopy
STP	Standard temperature and pressure
TER	Threshold elemental ratio
TGA	Thermogravimetric analyzer
TOR_i	Thermal oxidative recalcitrance
UCPy	Uncontrolled pyrolysis
VM	Volatile matter
WEF	Water-extractable fraction of biochar
WS	Walnut shells
XRD	X-ray diffractogram
ζ potential	Zeta potential

Introduction

Emerging economies such as Ukraine, Chile, China, India, and Turkey lead the global production of walnuts, reaching a total of ~ 1.47 million metric tons per year as of 2021 (USDA 2022). For these countries, Europe is one of the largest export destinations for walnuts. European walnut imports increased at an annual rate of 11% and the costs reached about €1.1 billion in 2017, with only 27% of these imports being unshelled walnuts (CBI 2019). Furthermore, the market value of shelled walnuts (walnut kernels) is about 4–5 times more than unshelled walnuts (Hussain et al. 2018). Due to high domestic processing costs, even walnuts cultivated in developed countries such as France are exported to Moldova for shelling and then reimported to minimize the walnut processing costs (CBI 2019). Thus, sustainable valorizing of walnut shells (WS) can help, to an extent, in offsetting the cost of shelling which itself is a complex and resource-intensive process (Wang et al. 2022).

Terra preta is the ancestor of anthropogenic pyrolytic carbon, also called biochar. Although the exact method of its preparation is still unknown (Woods et al. 2009), the consensus is that it was first made by the tribes in the central amazon, between 60 and 1640 AD, by the slow burning of refuse organic matter (combined with charcoal) under soil without thermochemical reactors for process control (Glaser and Birk 2012). Biochar derived from the pyrolytic conversion of WS is a value-added product that has demonstrated potential for environmental applications such as carbon sequestration (UN SDG indicator 13.2.2), soil amelioration (UN SDG 15.3.1), and liquid-phase adsorption (UN SDG 6.3.1) (Duan et al. 2017; Uslu et al. 2020; Li et al. 2020b). WS is a lignin-rich feedstock that maximizes char production and shows less catalyzing or inhibiting effects from ash and alkali and alkaline earth metals (AAEM) as compared to other refuse biomass such as crop residues and industrial/sewage sludge (Nair et al. 2020). Biochar is usually produced through controlled pyrolysis (CPy) where process parameters such as inert-gas purge, heating rate, and/or highest treatment temperature (HTT) are controlled (Uslu et al. 2020; Qiu et al. 2018). This leads to complex thermochemical control systems and expensive processes. Capital investment in pyrolysis control equipments contribute a large proportion of production cost, which ranges between 98 and 353 US$ Mg^{-1} of biochar (Ahmed et al. 2016; Dickinson et al. 2015). Hence, more research is needed to lower biochar generation costs and render this market financially and technically accessible in the long term, especially in emerging economies. To this effect, biochar production from uncontrolled pyrolysis (UCPy) can play a significant role. Then, the key issues are gaseous emissions from UCP_y and the suitability of resultant biochar for environmental applications such as carbon sequestration, soil amelioration, and pollutant adsorption.

The previous decade has also witnessed numerous research to hybridize pristine biochar for advanced applications. One such variant is magnetic biochar that is synthesized through impregnation-pyrolysis, chemical co-precipitation, and reductive co-deposition of transition metal compounds (Fe, Co, Ni, etc.) on the biochar matrix. This strategy facilitates the separability of biochar from aqueous media after adsorption (Li et al. 2020a; Wang et al. 2014). Furthermore, the presence of transition metal compounds in magnetic biochar can also give rise to other capacities such as catalytic degradation of pollutants, and photocatalytic carriers (Yi et al. 2020). Out of the various magnetization methods, ex-situ chemical co-precipitation is an easily controllable, cost-effective, and simple method for achieving a high saturation magnetization as well to improve adsorption capacity, and surface charge (Thines et al. 2017.). In the context of the present work, it will be important to test whether and how the ex-situ magnetization method alters the

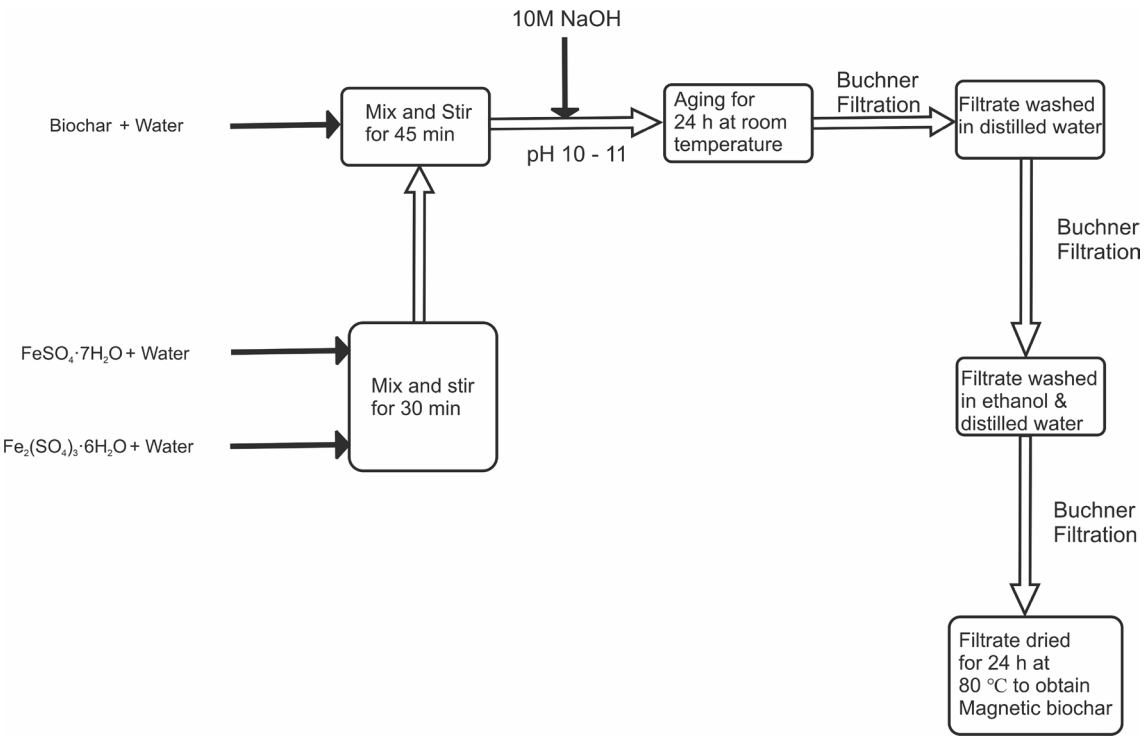

Fig. 1 Scheme showing the manipulations to obtain magnetized WS biochar through chemical co-precipitation with iron salts

Table 1 Varying amounts of iron sulfate solutions used for preparing magnetic walnut shell biochar

BWS0 (unmagnetized)	Iron sulfate solutions				Name of magnetic Biochar
Initial mass	$FeSO_4.7H_2O$	Water	$Fe_2(SO_4)_3.6H_2O$	Water	
g	*g*	*ml*	*g*	*ml*	
50	20	150	18.5	1300	BWS1
50	15	113	12.5	879	BWS2
50	10	75	8.5	598	BWS3

physico-chemical characteristics of the carbon matrix that was derived by UCPy of WS.

The environmental functions of biochar are heavily influenced by its physical and chemical characteristics, which, even for the same feedstock, can vary significantly depending on the synthesis route and hybridization method (Wu et al. 2012; Amin et al. 2016). Hence, a comprehensive quantitative and qualitative characterization of any biochar is crucial for its environmental application (Igalavithana et al. 2018). Herein, WS biochar is prepared via UCPy using an off-the-shelf pyrolysis oven and is then magnetized through an ex-situ chemical co-precipitation with iron salts. This article aims to systematically investigate and compare the physico-chemical properties of WS biochar and its magnetic derivatives, and the properties of the water-extractable fraction of these biochars concerning their utilization in carbon sequestration, soil amelioration, and liquid-phase pollutant adsorption.

Experimental

Pyrolysis process

The WS (*Juglans regia* L.) were collected from Bad Münder am Deister, Lower Saxony (Germany), and solar dried for 24 to 48 h. The fiber and elemental analysis of WS were carried out by LUFA Nord West GmbH. The WS were then pyrolyzed in a garden-scale pyrolysis oven manufactured by Sagawe & Sohn GbR (Hameln, Germany). The stainless-steel oven is 0.89 m high with a pyrolysis chamber volume of 14 L. The images of this unit and pyrolysis process are in Figure S1 supplementary material. During the pyrolysis, mineral insulated thermocouple type 12, K (NiCr/NiAl) with 4-channel datalogger SE-521, TC-direct GmbH (Mönchengladbach, Germany) were used to record the ambient and the core temperature (at about 0.10 m from the oven base). On average, for a 3 kg input mass per pyrolysis trial, the process takes about 1.3 h with the HTT reaching ~ 690 °C. The carbonized biomass was quenched in rainwater (TOC of 4.11 mg/L) and solar dried for 2 days. The resulting biochar from three such trials was mixed, oven dried at 105 °C for 24 h, and shredded at 8000 rpm to 0.2 mm in a ZM 200 centrifugal mill manufactured by Retsch GmbH (Haan, Germany) and was termed as BWS0.

Preparation of magnetic biochar

All glassware was washed in distilled water. About 50 g of BWS0 was first oven dried at 105 °C for 24 h and then treated with $FeSO_4 \cdot 7H_2O$, $Fe_2(SO_4)_3 \cdot 6H_2O$ and distilled water at room temperature (between 21 and 23 °C). The detailed scheme is shown in Fig. 1. By altering the amount of incorporated iron salts, three different magnetic WS biochars were prepared (Table 1).

Chemical assays

C, H, N, O, S, and Fe analysis

The analyses of C, H, N, O, S, and Fe in the biochar were done by Mikroanalytisches Laboratorium Kolbe GmbH (Fürth, Germany). The measurement uncertainty was ± 0.01% for C, H, N, ± 0.015 for S, and ± 0.012 for Fe. In short, biochar samples were weighed and dried overnight at 105 °C. The C, H, N, and O percentage in biochar is measured in the Vario Mikro Cube C, H, N analyzer (Elementar, Frankfurt, Germany). Sulfur was measured after combustion in a Mitsubishi AQF-2100H using a Model 883 ion chromatograph (Metrohm AG, Herisau, Switzerland). After digestion in a MARS 6 microwave digestion system (CEM, North Carolina, USA), Fe was measured using an Arcos ICP-OES (SPECTRO Amtek, Kleve, Germany). Here, O in magnetic biochar could not be measured due to interference from the Fe as it is bound as oxides and is not released despite a combustion temperature of 1400 °C. Hence, O is determined by subtracting the sum of elemental analysis and ICP-OES from 100 dry wt.-%.

ICP-OES analysis

For the analysis of different elements in the biochar, the samples were analyzed by inductively coupled plasma optical emission spectrometry (ICP-OES) (iCAP 6000 ICP Spectrometer, Thermo Fisher Scientific Corporation, Waltham, Massachusetts, USA). For this, about 30 mg of

powder from each sample was incinerated for a minimum of 8 h in a muffle furnace (M104, Thermo Fisher Scientific Corporation, Waltham, Massachusetts, USA). After cooling the samples to room temperature (RT) (between 21 and 23 °C), 1.5 ml of nitric acid (Rotipuran® Supra 69%, diluted 1:3 in ultrapure water) was added. After 10 min 13.5 ml of ultrapure water was pipetted to the samples. The solutions were filtered (0.45 µm pore size, Carl Roth, Karlsruhe, Germany) and stored in vials at − 20 °C before final analysis. A rate of ≤ 100% indicates retention and that above 100% corresponds to an enrichment of an element in the resulting biochar (Karim et al. 2018), as calculated using Eq. (1).

$$\text{Retention rate (\%)} = \frac{\text{element conc. in biochar}}{\text{element conc. in biomass}} \times \text{biochar yield (\%)} \quad (1)$$

ATR-FTIR

Mid-IR spectra between 4000 and 400 cm^{-1} were collected with Nicolet iS50 (Thermo Fisher Scientific Corporation) having a KBr beam splitter, diamond crystal, and deuterated triglycine sulfate (DTGS) detector. The measurement parameters of optical velocity, gain, and aperture size were 0.1581, 2.0, and 87, respectively. A total of 32 scans at resolution 2 cm^{-1} were collected for each sample and averaged. The ATR peak intensities were dependent on the refractive index of the crystal and sample (Volkov et al. 2021), which could be changed after magnetization. Hence, peak intensities were not used for semi-quantitative estimation of the amount of each functional group present.

Thermal oxidative recalcitrance (TOR_i)

In summary, 5 mg of each sample was combusted using aluminum oxide crucibles (70 µL) in a TGA/DSC 3 + /LF (Mettler Toledo, Ohio, USA). The apparatus was operated at a temperature range from 25 to 1050 °C under an O_2 flow (purity of 99.999% procured from Linde Gases GmbH) of 40 mL/min and a heating rate of 10 °C/min. Triplicate measurements were made for all samples and averaged. The TOR_i, is evaluated according to (Nair et al. 2020) in MATLAB R2020b with BWS0 as the reference material.

Proximate analysis of biochar

The volatile matter (VM), ash content (AC), and fixed carbon (FC) were measured through proximate analysis in TGA (same equipment in "Thermal Oxidative Recalcitrance (TORi)" section) based on (Garcia et al. 2013; Aller et al. 2017). At first, 10 mg of each sample was pre-purged in an N_2 flow of 40 ml/min for 10 min at 30 ℃. Residual moisture was removed isothermally at 110 ℃ for 15 min in an N_2 atmosphere. Then, the sample was linearly heated (70 °C/min with 40 ml/min N_2) and kept isothermal at 950 °C for 10 min to volatilize VM. The sample was cooled and then kept isothermally at 550 °C for 20 min in O_2 (40 ml/min) to evaluate loss on ignition. Finally, the sample was cooled to 110 °C in N_2 (40 ml/min) and kept isothermal for 15 min. Samples were measured in triplicates and averaged. The data were evaluated using MATLAB R2020b.

Labile C, N, and P

For each biochar, VM was first removed as per "Proximate Analysis of Biochar" section. Then the C, N, and P contents were determined as in "C, H, N, O, S, and Fe Analysis" section. Based on the elemental measurements of biochar and that of biochar deprived of VM, the C, N, and P of the labile VM in the biochar after pyrolysis were evaluated. A conventional TOC determination where the inorganic carbonates are removed with 1 M HCl was not utilized as it would report the entire carbon in the biochar as microbial-accessible labile organics.

Py-GC–MS

The pyrolysis–gas chromatography-mass spectroscopy (Py-GC–MS) of BWS0 was performed with a double shot Pyrolyzer EGA/PY-3030D (Frontier Laboratories Ltd., Fukushima, Japan) attached to a Trace 1310 GC and ISQ 7000 Single quadrupole MS System from Thermo Fisher Scientific. About 15 mg of the samples were placed in small crucibles and introduced into the furnace via an autosampler (AS-1020E, Frontier Lab). The flash pyrolysis was performed at 800 °C and evolved gases were then directly injected into the GC/MS system for analysis. The gas chromatograph was equipped with a low-to-mid polarity Ultra Alloy® capillary column (UA^+-5, F-Lab.) of 30 m × 250 µm × 0,25 µm film thickness. The carrier gas was helium at a controlled flow of 1 ml min^{-1}. Total ion current chromatograms (TIC) were acquired at 70 eV ionizing energy. The obtained mass chromatograms of substances were analyzed and compared with NIST and F-Search (F-Lab) databases. The detected compounds were semi-quantified using area normalization of TIC peaks from five.

Physical and structural characterization

Powder X-ray diffraction (PXRD)

PXRD was carried out by using a Stadi P transmission diffractometer (Stoe, Darmstadt, Germany) operating with Ge

(111)-monochromatized CuKα1 radiation (λ = 1.54056 Å) and a position-sensitive Mythen 1 K Detector.

Raman analysis

Raman spectra were measured with a Senterra microscope (Bruker, Massachusetts, U.S.A). The used laser has a wavelength of 532 nm with a power of 0.2 mW and a resolution of 3–5 cm^{-1} (Wang et al. 2011; Yin et al. 2018). The integration time was 2 s and two loops were performed per measuring point.

Magnetic properties

The magnetic hysteresis at room temperature was measured using a Model 7407 Vibrating Sample Magnetometer (Lake Shore Crytronics, Ohio, USA). Runs were performed as a sweep from no field to a maximum of 7000 G in both directions at a ramp rate of 70 G. The magnetic flux density (emu/g) vs magnetic field (Oe) was plotted based on sample mass for hysteresis calculations.

Scanning electron microscopy (SEM)

SEM measurements were made using Quanta 200 (FEI, Oregon, USA) after degassing in N_2 (for 6 min to 8 min) and gold coating (at 25 mA for 2 min) the samples in Edwards S150A sputter coater. Vacuum conditions for the electron gun were kept below 8.7e-005 mbar. The micrographs were captured at 12 kV and 15 kV at resolution 4 and different magnifications (values) for different samples.

N_2 Physisorption measurements

Surface area and pore characteristics were measured by nitrogen gas sorption at 77 K in NOVA 3200e (Quantachrome Instruments, brand of Anton Paar, Boynton Beach, Fl) according to IUPAC guidelines (Thommes et al. 2015). Before measurements, biochar was degassed in a vacuum at 100 °C for 24 h. The surface area was calculated using multipoint Brunauer–Emmett–Teller (BET) ($0.03 \leq P/P_o \leq 0.1$; equilibrium time of 120 s; 7 adsorption points) and pore size distribution through DFT analysis ($0.006 \leq P/P_o \leq 0.94$; equilibrium time 120 s). The software used was NovaWin 11.4. For the DFT fit, a NLDFT equilibrium model with both slit and cylindrical pores was used. All correlation coefficients of BET calculations were larger than 0.99.

Zeta potential and point of zero charge

The zeta potential (ζ) is the potential at the plane of shear/sliding plane in the electrochemical double layer at the colloid-solution interface. The pH where the surface becomes uncharged is the point of zero charge (pH_{pzc}) in presence of H^+ and OH^- as the only potential-determining ions. Biochar was mixed with ultrapure water from Arium Mini (Sartorius AG, Göttingen, Germany) at a ratio of 1:5 and stored for 48 h. The ζ was analyzed using ZetaPALS (BrookHaven Instruments Corporation, New York, USA) based on ref (Verma and Singh 2019). For each sample, 5 runs (10 cycles per run) were performed and averaged. Similarly, to determine the pH_{pzc} the ζ of BWS0 was also measured at six different pH (3.0 – 11.5) adjusted by dropwise addition of 0.1 M NaOH and 1 M HCl.

Water-extractable fractions (WEF)

Extraction method

The extraction method is based on ref (Zhang et al. 2014). The glassware was rinsed with ultrapure water from Arium Mini (Satorius, Göttingen, Germany) prior to extraction. Similarly, syringe filters were also washed with 50 mL of ultrapure water. Biochar was mixed with ultrapure water at a ratio of 10 mg to 1 ml to prepare a 45 ml solution. Then, the solution was stirred (150 to 200 rpm) for 3 h. Then, the samples were stored in a dark container for 24 h. Subsequently, the suspension was filtered using a 0.45 µm syringe filter (CHROMAFIL® Xtra Hydrophilic PES membrane). The resulting supernatant (water-extractable fraction) was used for the following measurements.

pH and electrical conductivity (EC)

After calibration of pH at 4, 7, and 10, a multimeter (WTW MultiLine® Multi 3630 IDS SET F/ SenTix® 940/ TetraCon® 925/ FDO® 925) measured pH and EC in duplicates and the resultant values were averaged. The solution had an average temperature of 18 °C.

Dissolved organic carbon (DOC)

DOC was measured as non-purgeable organic carbon (NPOC) using Vario TOC cube (Elementar Analysensysteme GmbH, Langenselbold, Germany). The measurement uncertainty of the equipment was 2%. About 0.2–0.5 ml/sample was introduced for combustion at 850 °C and the CO_2 was measured through IR detection. Carrier gas flow was 200 ml/min. The known standard used for calibration was 5 ppm and 20 ppm of potassium hydrogen phthalate. The calculations were performed using the software Vario TOC Software version 4.0.12. The standard followed was DIN EN 1484.

Table 2 Elemental and fiber analysis of dried walnut shell biomass

#	Amount	Unit	Measurement standard
α-Cellulose	35.5	Dry wt.-%	ASU F 0084; 2011–06; #1
Hemicellulose	12		VDLUFA III 6.5.3; 2012; #1 and
Lignin	40.3		VDLUFA III 6.5.1; 2012; #1
C	47.8		DIN 51,732; 2014–07
H	6.60		
N	0.22		
O	45.2		
S	0.01		DIN EN ISO 11885 (E 22)
P	0.01		DIN EN ISO 11885 (E 22)
H/C	1.64	Molar ratio	
O/C	0.70	Molar ratio	
K	0.25	Dry wt.-%	DIN EN ISO 11885 (E 22); 2009–09
Na	< 0.01		
Mg	0.02		
Ca	0.18		
Fe	0.014		
Si	0.062		

Table 3 Proximate analysis results, thermal oxidative recalcitrance (TOR_i), and ash-free fixed carbon of walnut shells (WS) and the biochars derived from them

Sample	Volatile matter %-dry-wt	Ash %-dry-wt	Fixed carbon (FC) %-dry-wt	FC (ash-free basis) %-dry-wt	TOR_i
WS	79.33	0.8	19.87	20.03	− 0.27
BWS0	10.04	3.41	86.55	89.60	0
BWS1	18.41	22.94	58.65	76.11	0.45
BWS2	17.05	17.99	64.96	79.21	0.44
BWS3	16.82	32.42	50.77	75.12	0.43

Table 4 Elemental analysis of unmagnetized and magnetized biochar derived from WS. Units are in dry.wt-%

Biochar	Total C %	C_{org} %	H %	N %	O %	S %	Fe %
BWS0	90.14	81.98	1.11	0.77	6.78	0.01	0.16
BWS1	71.40	55.34	1.30	0.42	N.D	0.13	11.04
BWS2	76.54	63.88	1.63	0.86		0.15	8.30
BWS3	74.69	56.91	1.82	0.79		0.83	5.05

UV–Vis spectroscopy

The spectra of samples in single-use cuvettes (path length, l = 10 mm) were collected between 200 and 900 nm using DR6000 UV–VIS spectrophotometer (Hach, Colorado, USA). Duplicate measurements were averaged. $SUVA_{254}$ (an indicator of DOM aromaticity) and E2/E3 (ratio of UV absorbance at 254 to 365 nm is inversely proportional to the molecular weight of DOM) were evaluated (Zhang et al. 2020b). Due to interference from inorganic ions below 230 nm, ratio of UV absorption at 254 and 204 nm was not calculated to estimate the fraction of saturated carbon in DOC (Li and Hur 2017).

Analysis of cations and anions

About 10 mL of the supernatant was used to measure the cations (K^+, Na^+, Mg^{2+}, Ca^{2+}, and NH_4^+) and anions (Cl^-, SO_4^{2-}) in an ion chromatograph (Dionex Aquion / Dionex Integrion HPIC with Dionex AS-AP autosampler (Thermo Scientific). The eluents used for cations and anions were 30 mM methane sulfonic acid and 4.5 mM Na_2CO_3/1.4 mM $NaHCO_3$, respectively. The detection method for analysis was conductivity with chemical suppression. Data analysis was performed using Chromeleon (v 7.2.10). Other measurement parameters are shown in Table S1.

Results & discussion

Elemental and fiber analysis

The elemental concentration and fiber content in the walnut shells (WS), *Juglans regia* L., are shown in Table 2. WS is primarily composed of lignin and α-cellulose, and only 12 wt.-% of hemicellulose. Similar compositions of WS is also reported in refs (Yuan et al. 2020; Kambarova and Sarymsakov 2008). However, in some other investigations (Altun and Pehlivan 2012; Senol 2021), higher hemicellulose concentrations similar to that of α-cellulose are found. Such differences arise from climatic and plantation conditions, walnut cultivars, and, to an extent, differences in measurement methodologies. In general, WS has one of the highest lignin concentrations (30 to 50%) compared to other crop residues and woods (Pirayesh et al. 2012) due to the lignification of the walnut endocarp. The presence of higher lignin and cellulose contents indicates a higher quantity of sclereids and increased shell thickness during fruit development. In our material, the shell thickness of WS is ~ 1–1.2 mm. As a pyrolysis feedstock, WS differs from the mineral- and ash-rich waste biomass (MWB) that the present authors have previously investigated (Nair et al. 2020) because WS has a) higher O/C molar ratio due to the phenolics in lignin and cellulose, b) higher organic carbon content, c) smaller concentration of AAEM, silicates, and ash, which lower the chances for catalytic pyrolysis, and d) trace amounts of Fe (0.014 wt.-%).

Chemical assay of biochar

Pyrolysis of WS has reduced the VM and increased the FC in BWS0. Compared to biochar from mineral-rich feedstocks (Isaeva et al. 2021), BWS0 has only 3.41 wt.-% ash (AC). The results from proximate analysis and TOR_i of WS and its biochar are shown in Table 3 while their elemental concentrations (CHNOS and Fe) in dry wt.-% are presented in Table 4.

Magnetic biochar has higher ash concentrations due to the presence of iron oxides. The Fe content in biochar follows the same trend as the amount of iron salts induced during chemical co-precipitation—BWS1 > BWS2 > BWS3. However, the ash concentration in BWS3 is larger than that for BWS2, which indicates possible impurities in BWS2 (to be discussed later). Magnetic biochars also possess larger VM release from the biochars and are observed as the increase in the DTG peaks of magnetized biochar compared to BWS0 at ~ 800 °C (Figure S2). The DTG peak of BWS3 during combustion is smaller than that of BWS2 due to lower ash content in BWS3. FC

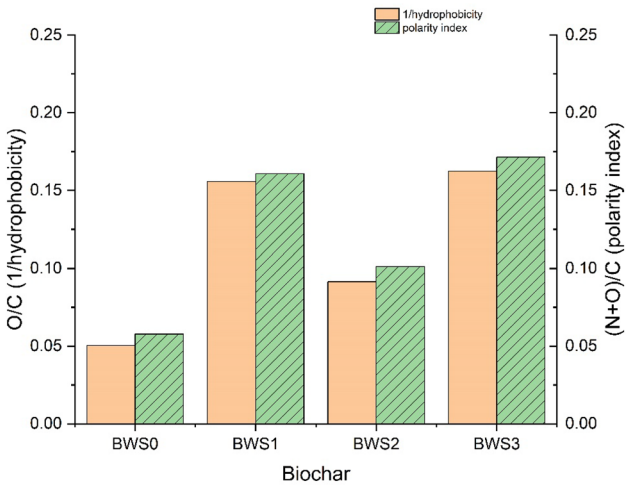

Fig. 2 O/C or 1/Hydrophobicity and (N + O)/C or polarity index of WS-derived biochars (at temperature ~ 690 °C) before and after magnetization

(ash-free basis) has also comparatively reduced after the incorporation of iron oxides. Hence, as seen in other studies (Zhao et al. 2013; Leng et al. 2019; Wurzer and Masek 2021), FC cannot be used as an indicator of the degree of carbonization in biochar when it undergoes post-pyrolysis chemical impregnations. With BWS0 as the reference, the TOR_i of all magnetized biochars are near 0.45 owing to an increase in their thermal oxidization stability relative to the pristine BWS0. However, the changes in the amount of iron infused do not seem to considerably change its oxidative stability.

The pyrolysis of walnut shell yields 28.5 wt.-% BWS0 with a total carbon and organic carbon of 90.14 and 81.98 wt.-%, respectively. BWS0 also has low hydrogen and oxygen, showing a good degree of carbonization and polycondensation of the material. The higher heating value of BWS0 calculated according to elemental (Channiwala and Parikh 2002) and proximate measurements (Parikh et al. 2005) are 31.99 and 32.14 MJ/kg, respectively. This high HHV is similar to that of Anthracite despite being produced from UCPy. The intrinsic accumulation of Fe in the unmagnetized BWS0 is small (0.16 wt.-%). BWS0 has a H/C_{org} and O/C_{org} molar ratio of 0.161 and 0.06, respectively. This fits within the definition (Eq. (2)) of biochar by the International Biochar Initiative (IBI) and the European Biochar Commission (EBC) (Budai et al. 2013; EBC 2012).

$$\frac{H}{C_{org}} \leq 0.7; \frac{O}{C_{org}} \leq 0.4 \tag{2}$$

$$BC_{+100} = -74.3 \times \frac{H}{C_{org}} + 110.2 \tag{3}$$

$$\mathrm{CSP} = \frac{BC_{+100}}{100} \times \left(\text{Yield of } C_{org}\right)_{biochar} \times \frac{44}{12} \quad (4)$$

The carbon sequestration potential (CSP) (Sieng-Huat 2019) of BWS0, calculated according to Eq. (4) is 0.84 $kg_{CO2}/kg_{biomass}$ for a BC_{+100} of 98.23% (Eq. (3)). BC_{+100} is the percentage of sequestered carbon remaining in the soil after 100 years. It can mitigate the N_2O emissions from the soil by ~ 73 ± 7% (Cayuela et al. 2015). For $H/C_{org} \leqslant 1$, this molar ratio can be correlated with an n*n aromatic cluster size (Eq. (5)), which predicts that BWS0 can have up to a maximum of 11-ring polyaromatic compounds, which is common for cellulose and lignin-rich materials at high HTTs (Xiao et al. 2016). It is not possible to draw such inferences from H/C_{org} molar ratio for magnetized biochar because of the changes in elemental concentrations (Fe, S, and H) introduced by the chemical co-precipitation. BWS0 has 92% aromatic carbon as measured from ^{13}C-NMR CP spectra between 165 and 110 ppm (Figure S3). Details of this ^{13}C-NMR analysis are in supplementary information.

$$\frac{H}{C_{org}} = \frac{2+4n}{2n^2+4n} \quad (5)$$

The O/C is inversely proportional to hydrophobicity and (N + O)/C is the polarity index, which increases with surface polarity (Zhao et al. 2019; Fan et al. 2018). These are shown in Fig. 2. Hydrophobicity is an important parameter relevant to biochar application. Adding hydrophobic biochar to soil can reduce its wettability, and water retention capacity, creating a preferential flow of contaminants to groundwater sources (Mao et al. 2019). Usually, low-temperature biochars (< 500 °C) are hydrophobic due to the presence of aliphatic functional groups, while at temperatures > 500 °C, hydrophobicity reduces due to the loss of these functionalities and the polarity arising from recalcitrant C-O, C = O and nitro groups on the turbostratic carbon, which assists in the formation of hydration clusters with water molecules. At higher HTTs, these oxygen and nitrogen functionalities also decompose due to polycondensation, and the biochar's affinity for water is limited to the adsorption on the well-developed micropores. BWS0 is more hydrophobic with a low O/C ratio compared to other pristine WS biochars produced through controlled pyrolysis at 600 and 700 °C as described in (Gupta et al. 2019; Lahijani et al. 2018). Magnetization resulted in a general increase in the hydrophilic nature due to the O-functionalities incorporated during the chemical co-precipitation. Hence, if land-applied, the magnetized variants may increase the water retention capacity of sandy and drought-prone soils (Suliman et al. 2017).

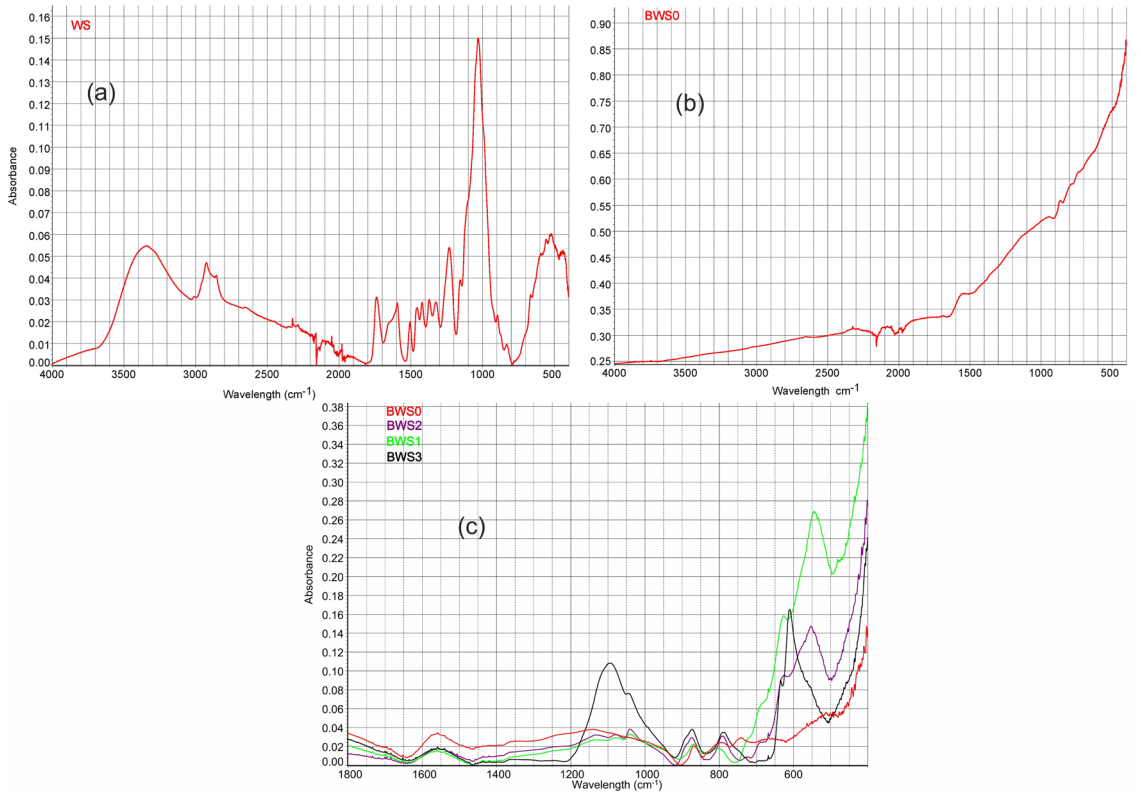

Fig. 3 ATR spectra of **a** WS between 4000 and 400 cm^{-1} **b** BWS0 between 4000 and 400 cm^{-1} and **c** of all BWS0, BWS1, BWS2, and BWS3 in the fingerprint region between 1800 and 500 $cm.^{-1}$

Unlike organic litter, a significant portion of the carbon, nitrogen, and phosphorus in biochar is recalcitrant. Some microbes, depending on conditions, can also mine energy and nutrients from such recalcitrant aromatic forms (Zhang et al. 2020a). Long-term incubation experiments would be required to quantify the fraction of recalcitrant carbon that is accessible by various types of soil microbes. Hence, in this study, to determine soil applicability from biochar properties, we consider that only the C, N, and P in the VM of biochar are immediately accessible to microbes. Therefore, labile C, N, and P in biochar were evaluated. There is no labile and readily plant-available phosphorous (P) in these biochars since P usually forms stable aromatics at HTT nearing 700 °C (Xu et al. 2016). However, BWS0 surface is negatively charged (seen in "Physical and Structural Properties of Biochar" section) at a pH of 9.45. Thus, it can adsorb Fe and Al ions, if present in the soil, to reduce their complexation with soil P; *ergo* not influencing the labile pool of P that may be present in the soil prior to biochar application. Under the assumption of homeostasis and carbon-controlled microbial communities, a higher soil loading rate of BWS0 can raise the net soil C/P (usually ~ 290) (Ch'ng et al. 2019) above the threshold elemental ratio of P ($TER_{C:P}$) creating a situation of P deficiency and energy (carbon) excess. $TER_{C:x}$ for a nutrient x defines the elemental ratio at which microbial activity switches from C limitation to a deficiency in x (Guo et al. 2020). This can incite microbial phosphatase synthesis by species from the genera *Pseudomonas*, *Bacillus,* and *Rhizobium*, and consequently improve P-mineralization (Pérez et al. 2007). In the long term, while C leaves the soil in the form of CO_2, mineralized P remains, and/or is turned into a plant-available form through microbial necromass. The absence of labile P is also beneficial to prevent runoff and subsequent eutrophication.

The molar labile C/N is 24.8, 62.3, 24.0, and 32.7 for BWS0, BWS1, BWS2, and BWS3, respectively. The soil molar C/N ratio for soil ranges from 10.2 to 30.2 (Tate 2020), with 24 considered a "balanced diet" (Brust 2019). Hence, BWS0 addition will not decrease the carbon use efficiency (CUE) as compared to other amendments rich in organic C. Magnetic biochar, on the other hand, is acidic with more Fe in it for soil P complexation. Thus, its application can make the soil P unavailable to plants. The C/N of BWS2 and BWS3 is also near the aforementioned optimal range for soil and is more hydrophilic than BWS0. However, their iron concentrations of > 5 dry wt.-% warrant further investigation into Fe speciation, and microbial toxicity.

WS shows strong signals in the IR region between 3500 and 2500 cm^{-1} (Fig. 3a). As seen in ref (Shah et al. 2018), these peaks mainly include the –OH stretching from lignin and carbohydrates near 3400 cm^{-1}, and –CH stretching vibrations at ~ 2930 cm^{-1}. These features disappear in the BWS0 (Fig. 3b) sample due to a reduction in $\nu_{(OH)}$, $\nu_{(NH)}$, and $\nu_{(CH)}$ vibrations (Singh et al. 2017) after carbonization. Figure 3c shows the comparative fingerprint region of IR spectra (between 1800 and 400 cm^{-1}) for the four biochars. After carbonization, the samples have lost most of the bands due to $\nu_{(C–O)}$ at ~ 1030 cm^{-1} that stem from polysaccharides. The peaks near 550 cm^{-1} and 634 cm^{-1} are from Fe–O stretching (Wan et al. 2020; Jack et al. 2019) of maghemite. Their relative peak heights change in proportion to the Fe content seen in elemental analysis—BWS1 > BWS2 > BWS3.

Table 5 Results from the ICP-OES analysis of WS-derived biochars and elemental retention/enrichment rate in BWS0

Elements	WS	BWS0	Retention rate in BWS0	BWS1	BWS2	BWS3
	mg/g	mg/g	%	mg/g	mg/g	mg/g
Al	0.028	0.186	186.70	0.023	0.022	0.048
B	0.047	0.155	93.17	0.018	0.012	0.039
Ba	0.002	0.007	86.68	0.004	0.004	0.005
Bi	0.005	0.244	1392.61	0.086	0.078	0.113
Ca	2.44	6.694	78.17	2.939	2.892	5.38
Cr	0.005	0.287	1504.87	0.102	0.094	0.135
Cu	0.013	0.027	59.42	0.003	0.003	0.011
K	1.152	4.025	99.56	0.857	0.755	2.84
Mg	0.051	0.112	63.01	0.052	0.045	0.038
Mn	0.011	0.027	70.84	0.009	0.01	0.011
Na	1.922	5.054	74.95	4.475	2.418	22.843
Ni	0.002	0.068	897.84	0.005	0.018	0.048
P	0.179	0.595	94.76	0.339	0.302	0.379
S	0.425	0.903	60.61	2.255	2.313	16.945
Sr	0.002	0.01	124.95	0.005	0.005	0.008
Zn	0.009	0.013	41.56	0.006	0.001	0.005

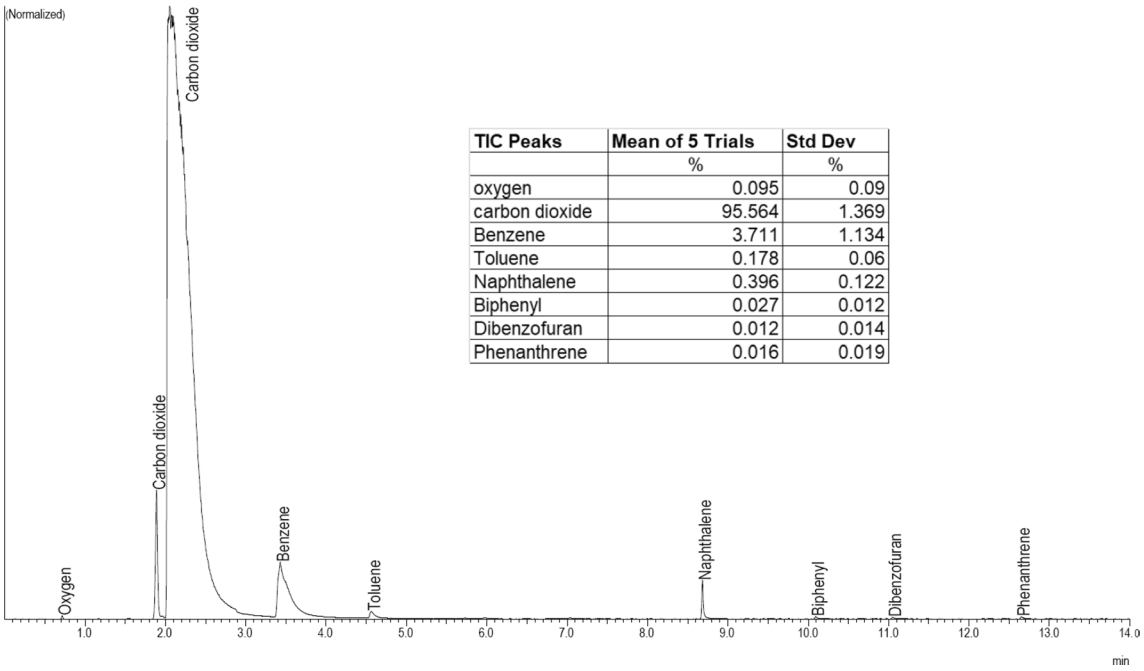

TIC Peaks	Mean of 5 Trials	Std Dev
	%	%
oxygen	0.095	0.09
carbon dioxide	95.564	1.369
Benzene	3.711	1.134
Toluene	0.178	0.06
Naphthalene	0.396	0.122
Biphenyl	0.027	0.012
Dibenzofuran	0.012	0.014
Phenanthrene	0.016	0.019

Fig. 4 Py-GC–MS chromatogram of BWS0 with a table showing compounds and gases evolved during analytical pyrolysis quantified using area normalization method

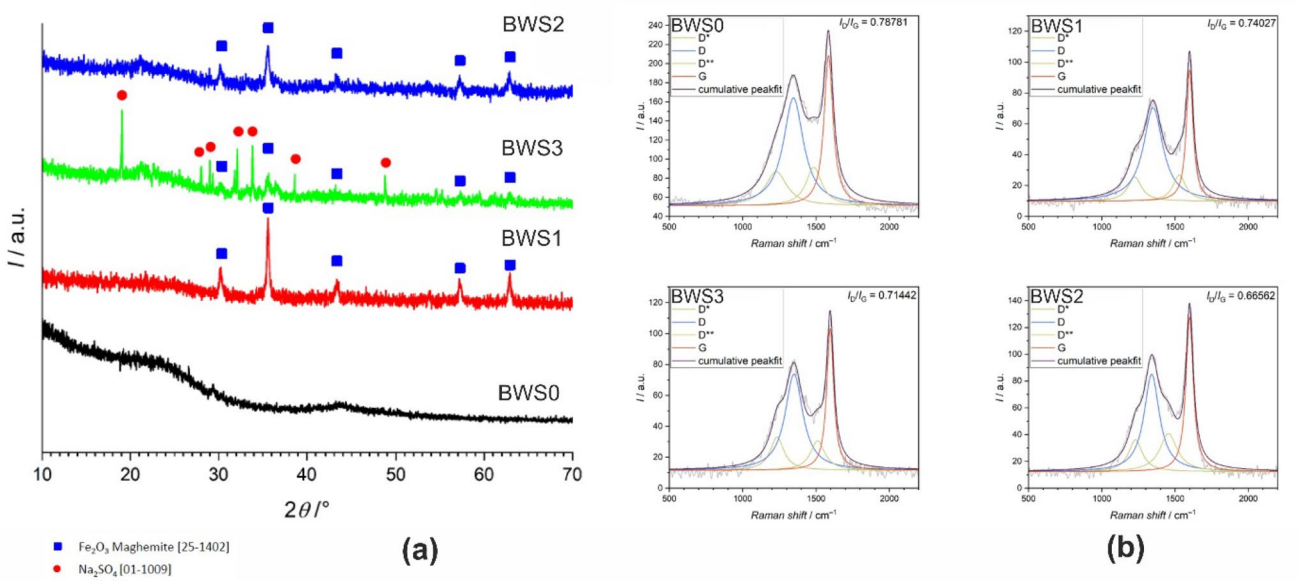

Fig. 5 **a** X-ray diffractograms of the WS-derived biochars BWS0 (unmagnetized) and BWS1-3 (magnetized) **b** Raman spectra of the biochars with Lorentzian 2-peak fits on the D and G bands

These peaks are absent in unmagnetized BWS0. Since the biochars are hydrogen-poor carbons (H/C < 0.3) (Russo et al. 2014) the presence of aliphatic carbon is quite weak and is only seen as a broad ridge between 1400 and 1000 cm^{-1}. The small peak at 670 cm^{-1} is from the Fe–O bond in magnetite. Trace amounts of silicates and phosphates do not contribute much to the region around 1000 cm^{-1}. The peak at 1600–1500 cm^{-1} is from $\nu_{(C=O)}$ of oxygenated functional groups (OFGs) such as carboxylic and carbonyl (Singh et al. 2017) that are acidic. The reactor environment during pyrolysis did not possess an active N_2 purge. This supports cracking reactions of tar and char in presence of the evolved

CO_2 and CO at high temperatures to remove more OFGs as compared to pyrolysis in a thermogravimetric reactor with N_2 purge (Hong et al. 2019). This would also explain the low O/C of BWS0 described above. The peaks at 1100 and 610 cm^{-1} present in BWS3 correspond to asymmetric stretching and bending vibrations of SO_4, respectively. As also later seen in PXRD, Na_2SO_4 is present as an impurity in BWS3. The peaks between 900 to 700 cm^{-1} arise from substituted aromatics.

Table 5 summarizes the concentrations of heavy metals and the amount of AAEM in the biochar and the elemental retention rate in BWS0. The concentrations of Cd, Co, Pb, and Se are negligible and below their detection limits. The concentrations of Ni, Zn, and Cu are below their respective lower guideline values (LGV) for abatement of ecological and health risks (Toth et al. 2016). Chromium in BWS0 is slightly above its LGV of 0.2 mg/g due to an enrichment of 1505%. Such enrichment of non-volatilizable elements is directly proportional to the highest treatment temperature and is unavoidable during pyrolysis. Carbonization has also increased Al, Bi, Ni, and Sr concentrations since these elements transformed into stable oxides or sulfides under 700 °C. Magnetic biochar has diluted heavy metal concentrations, ergo they lie below their LGV limits. In the case of AAEM, K is ~ 100% retained due to the lack of Cl providing a volatilization route during the active pyrolysis while a portion of Mg, Na, and S are lost. It is worth noting that the heavy metal enrichment in WS-based biochars is still considerably less than that from MWB like sewage sludge and manure (Liu et al. 2015; Zuo et al. 2020). Also, only the speciation of Cr can reveal whether it is phytotoxic or not accessible within the carbon matrix.

Figure 4 shows the Py-GC–MS chromatogram of BWS0, the mean and standard deviation of the concentration of the gases and compounds as a percentage of the total products evolved during analytical pyrolysis. Carbon dioxide and benzene constituted about 95.5 and 3.7% of the total chromatogram area, respectively. The detected PAH are naphthalene, biphenyl, and phenanthrene. These PAH, which are < 7–rings, are biodegradable (Rombolà et al. 2016) and can undergo biological or chemical oxidation as biochar ages.

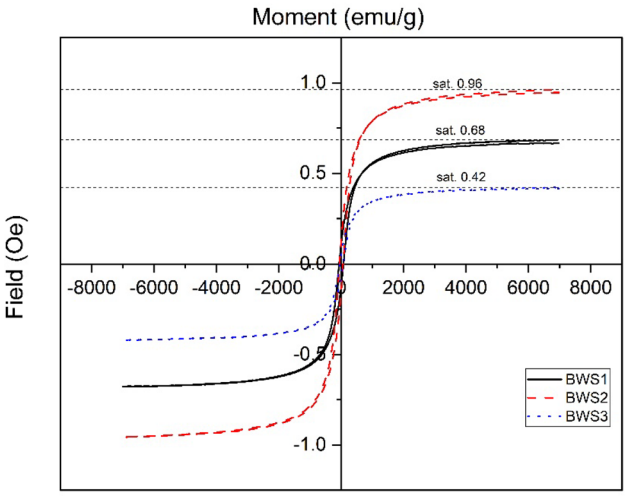

Fig. 6 Magnetic hysteresis curves of WS biochar containing magnetic iron oxide compounds

Physical and structural properties of biochar

The PXRDs and Raman spectra of the four biochar samples are shown in Fig. 5 a and b, respectively. The broad peaks in the PXRDs at 2θ of 23.5° (002) and 43.8 (101) indicate the presence of strongly disordered sp^2 amorphous carbon as that is expected from non-graphitized biochar. Diffraction peaks of γ-Fe_2O_3 can be found at 2θ of 30.1° (220), 35.5° (311), 43° (400), 57° (511), and 63° (440) (Golubev et al. 2019) in the magnetized biochar samples. For BWS3, in addition, the PXRD peaks of Na_2SO_4 are found which is in line with the FTIR results that indicated the presence of sulfate ions in this sample. Na_2SO_4 can be created during the co-precipitation process when using NaOH for initiating the precipitation process.

During carbonization, the intensity of the D band (I_D) at 1350 cm^{-1} in the Raman spectra represents defects in aromatic ring structures (which are absent in perfect graphite) while the G band (I_G) at 1590 cm^{-1} indicates (locally) ordered structures of carbon. The D* band arises from sp^3-bonded carbon atoms and the D** band is associated with sp^2-bonded carbon atoms as well as fragments or functional groups in the disordered structure (Yin et al. 2018). The I_D/I_G ratio of BWS0, BWS1, BWS2, and BWS3 are 0.79, 0.74, 0.67, and 0.71, respectively. Based on these ratios of I_D/I_G, the average size of ordered graphitic regions ("cluster size") can be calculated as the coherence length (L_a) according to the Eq. (6).

$$\frac{I_D}{I_G} = \frac{C(\lambda_L)}{L_a} \; : \; C(\lambda_L) = C_0 + (\lambda_L \times C_1) \tag{6}$$

Table 6 Pore characteristics—specific surface area determined by the BET method (S_{BET}) and pore volume (V_{pore})—of unmagnetized and magnetized WS biochars

Biochar	S_{BET} m^2/g	V_{pore} cc/g	DFT fit error %
BWS0	292	0.133	0.28
BWS1	227	0.157	0.361
BWS2	268	0.174	1.565
BWS3	239	0.164	2.126

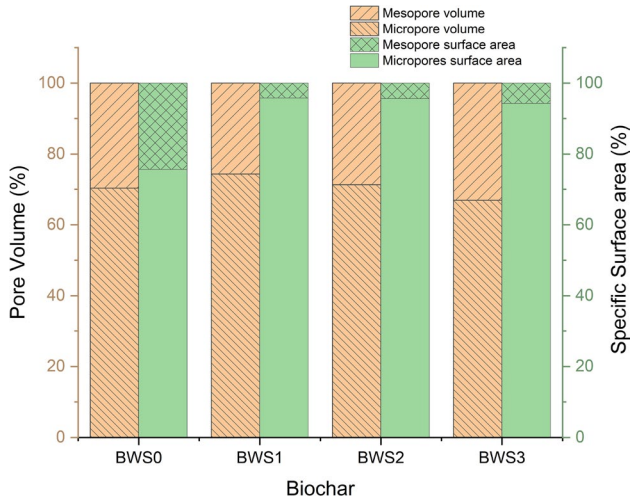

Fig. 7 Relative contributions of mesopores and micropores to the total pore volume and the total BET surface area in WS-derived biochar (BWS0 unmagnetized, BWS1-3 chemically magnetized)

where λ_L is the Raman excitation wavelength (532 nm); $C(\lambda_L)$ is a wavelength-dependent factor; and C_o and C_1 are constants (-12.6 nm and 0.0333, respectively) when 400 nm $< \lambda_L <$ 700 nm (Matthews et al. 1999). The L_a of BWS0, BWS1, BWS2, and BWS3 are 6.50, 6.91, 7.69, and 7.16 nm, respectively. For nanocrystalline graphene structure, I_D/I_G increases with the introduction of defects while for sp^2 amorphous carbon it decreases at higher defect density (Childres et al. 2013). BWS0elongs to the latter as seen from the XRD spectra. The magnetized biochars have more defects than BWS0 owing to the introduction of maghemite. Most of the magnetite formed from co-precipitation oxidizes to maghemite during the formation of magnetic carbon nano-particles. The absence of magnetite in Raman spectra (~690 cm^{-1}) and FTIR spectra confirms this.

The SEM micrographs depict the porous nature of BWS0 and the impregnation of iron oxide particles in the magnetic variants (Figure S4). Low concentrations of AAEM are not distinguishable in the images. The magnetic biochars are superparamagnetic (Fig. 6) with the ratio of magnetic remanence to saturation magnetization (M_s) of less than 25% (Cazetta et al. 2016). The M_s is less than 1 emu/g for all cases. This is lower than magnetite which tends to form during such chemical co-precipitation. The M_s of BWS3 seems to be an outlier since it is independent of the amount of iron introduced during synthesis. However, the magnetic WS biochar can be still effectively separated from the aqueous solution in the presence of an external magnetic field (Figure S5).

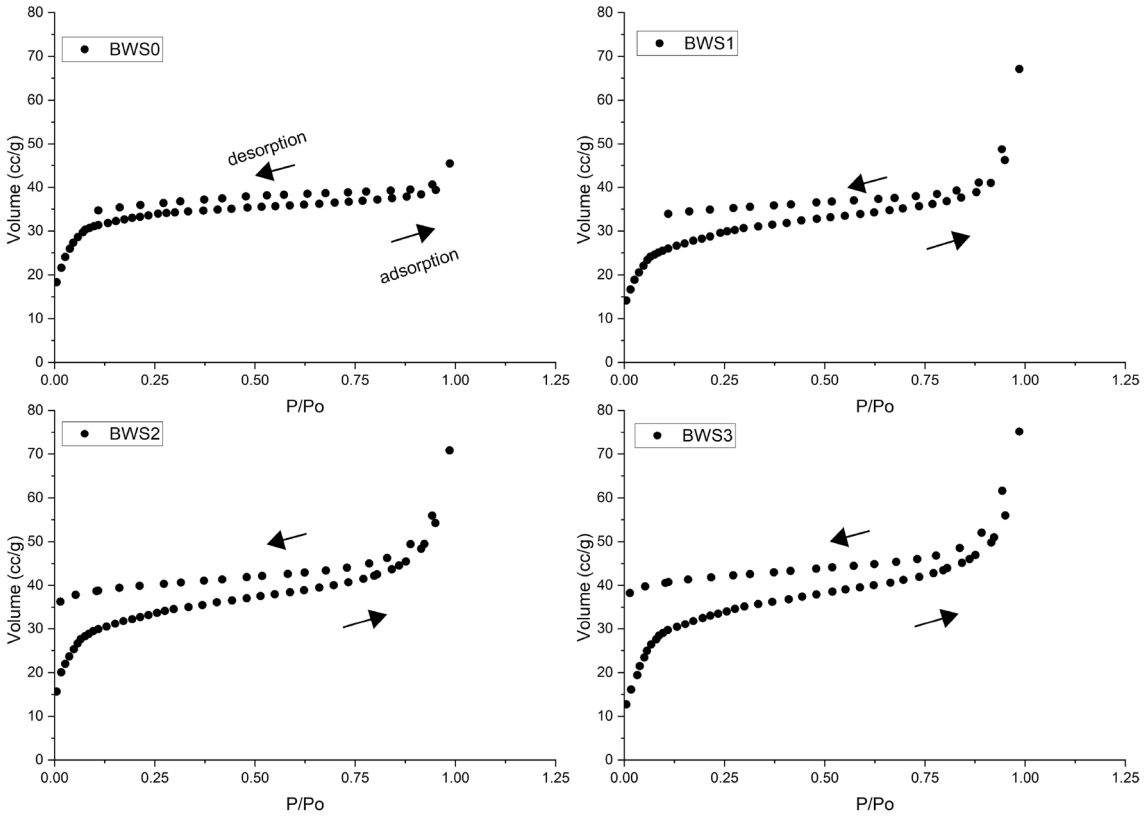

Fig. 8 N_2 adsorption–desorption isotherms of WS-derived biochars

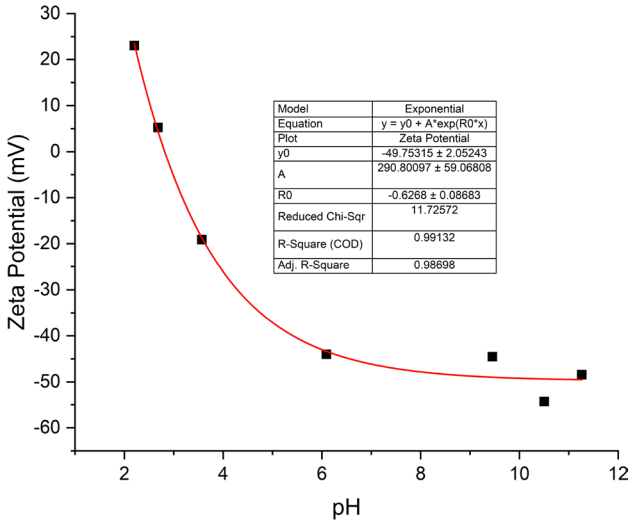

Fig. 9 Zeta potential (ζ) of BWS0 plotted against pH

The specific surface areas (S_{BET}) and pore volume (V_{pore}), as derived from nitrogen sorption measurements, of the biochars are shown in Table 6. The S_{BET} of BWS0 is comparatively larger than other WS biochar in literature (Lahijani et al. 2018; Kaya et al. 2020) which have been prepared through controlled pyrolysis at 700 °C. Expectedly, it is lower than those materials that have also undergone activation or washing as seen in refs (Qin et al. 2021; Wan et al. 2021).

Usually, there is an inflexion temperature (Leng et al. 2021) beyond which the porosity of biochar reduces with an increase in HTT due to pore collapse (from char melting, graphitic stacking, and pore fusion) or widening into macropores (reducing microporous surface area and increasing pore volume). The inflexion point for BWS0 obviously only occurs at temperatures > 700 °C (Lahijani et al. 2018; Qin et al. 2021). It is worth noting that this micropore collapse theory, though widely used for biochar derived from CP_y in inert environment, has its origins in activated carbon prepared under oxidizing conditions, which usually does not show an open-loop hysteresis curve during N_2 physisorption (Maziarka et al. 2021). In this study, despite the partial oxidation conditions, an open-loop hysteresis exists (seen later). Therefore, to confirm the existence of an inflection point due to pore collapse, a detailed investigation of possible adsorption-induced pore deformation is required. However, here, this would not be beneficial to the BWS0 synthesis because, in the case of an UCP_y, it is not possible to optimize biochar production based on inflection point.

The S_{BET} ($r > 0.99$) of BWS0 is higher (292 m^2/g) than the corresponding values of its magnetized counterparts, probably from pores blocked by iron oxide particles in the latter. These particles are introduced into the mesopores of the biochar during chemical co-precipitation. Hence, after the incorporation of iron oxides, the contribution from mesopores to the total surface area and pore volume reduces as seen in Fig. 7. The V_{pore} of magnetized biochars is higher than BWS0 due to the contribution by mesopores pores (2–50 nm) in maghemite.

The IUPAC's adsorption isotherms (Thommes et al. 2015) are used as a reference for interpreting the adsorption–desorption curves of biochar. The isotherms of the biochar in Fig. 8 are a blend of Type I (Langmuir) and Type IV. The steep rise at low relative pressures (P/P_o) for all samples indicates that during pyrolysis the micropores have developed. The adsorption corresponding to higher P/P_o shows the presence of mesopores, the amount of which varies with the amount of magnetizable material levels (Yang et al. 2016; Spokas et al. 2014). The N_2 adsorption also takes place in the larger mesopores introduced by the iron oxides and thus is higher in magnetized biochars. The larger hysteresis between the adsorption and the desorption branch introduced in magnetic biochars between 0.1 and 0.9 P/P_0 is also evidence of mesopores. The desorption time scale is much larger than that of the experiment and causes open-loop hysteresis, which may be caused by steric restrictions at the openings of micropores (Nguyen and Bhatia 2009). Such open-loop hysteresis curves are also known (Maziarka et al. 2021) to be caused by the deformation (swelling/contraction) of micropores in materials such as activated carbon during N_2 adsorption. This can be confirmed if the hysteresis disappears during CO_2 physisorption. The surface area should reduce with increasing levels of iron content due to pore blocking by iron oxides. However, BWS3 is an outlier which may be due to the presence of Na_2SO_4 in BWS3 as seen in "Elemental and Fiber Analysis" section.

The ζ potential of biochar is another surface property that plays an important role in soil application and adsorption. For BWS0, ζ potential increases with a reduction in

Table 7 Water-extractable fractions of WS-derived biochar: Concentrations of cations and anions, dissolved organic carbon (DOC), electrical conductivity, and results from UV–VIS analysis ($SUVA_{254}$ and E2/E3)

WEF parameters	Unit	BWS0	BWS1	BWS2	BWS3
Cl^-	mg L^{-1}	8.11	5.01	5.42	7.68
SO_4^{2-}		3.97	29.54	21.83	155.07
NH_4^+		1.32	0.32	0.35	1.32
Na^+		8.20	17.56	14.89	79.48
K^+		30.49	3.59	2.82	11.16
Mg^{2+}		0.68	0.68	0.59	0.68
Ca^{2+}		3.98	3.97	3.60	8.33
DOC		19.75	156.38	296.45	191.46
EC	dS m^{-1}	0.20	0.12	0.11	1.22
$SUVA_{254}$	L mg^{-1} m^{-1}	0.50	0.13	0.01	0.03
E2/E3	ratio	5.00	18.89	8.00	21.50

pH as shown in Fig. 9. The pH_{pzc} of BWS0 is 2.81, corresponding to an acidic surface. This is due to the absence of an inert N_2 purge to remove evolved gases away from the pyrolyzing substrate. Consequently, the biochar can undergo oxidation to form acidic surface functional groups such as carboxyl and carbonyl groups. Their dissociation in water leads to a ζ of − 44.5. Such a steep fall in pH_{pzc} is also seen during the oxidization of activated carbon surfaces (Álvarez-Merino et al. 2008; Jaramillo et al. 2010). BWS0 thus shows an electrostatic affinity for cations in a wide pH range between 2.8 and 9.45. The ζ potential of magnetic variants BWS1 (− 32.17 mV), BWS2 (− 18.34 mV), and BWS3 (− 39.92 mV) have not changed to the positive range despite the introduction of iron oxides (Long et al. 2019). Iron oxides impart positive charges through the formation of complexes with OFGs increasing the disorder of the carbon structure and inducing surface porosity; to a lesser extent by physical coverage of iron oxides on the biochar surface (He et al. 2020). The electric charge of magnetic biochar can be traced back to three causes: a) deprotonation of the acidic OFGs in the magnetized biochars offsets the positively charged iron moieties; b) the conjugated π-aromatic structure can act as electron donors or acceptors due to the polarization of basal plane near the edge defects created by the OFGs and c) contribution of negative charge from adsorbed sulfates, carbonates and phosphates to a small extent (Xu et al. 2020; Verma and Singh 2019). The stability and dispersibility of colloids increase when ζ potential < − 30 mV. So, except for BWS2, there exists a potential for biochar-induced groundwater contamination (through colloid-enabled transport of contaminants) from the sub-surface depending on the net pH and EC of the soil medium. The low pH_{pzc} and high pH of BWS0 enable applicability in a wide range of complex dispersion mediums, including as a sink for cations when added to most soils (pH 4.7–5.5) (Zhao et al. 2015).

Water-extractable fractions (WEF)

The result from ion chromatography, DOC, and EC measurements, reflecting the substances leaching from the biochar, are shown in Table 7. The concentrations of leaching anions PO_4^{3-} and NO_3^- are very low because of the formation of their recalcitrant forms such as pyrophosphates (Sahin et al. 2017) and binding to the biochar matrix, respectively, and hence below the quantification limit of the instrument. As seen earlier, the investigated biochars have no readily plant-available P. EC is directly proportional to the concentrations of monovalent and divalent water-soluble ions and is high for BWS3 (1.22 dS m^{-1}) and BWS0 (0.2 dS m^{-1}).

The EC-value below 4 dS m^{-1} for all biochar suggests that they will not increase soil salinity after land application (Carrier et al. 2012). In BWS0, Ca^{2+} and Mg^{2+} are lower than K^+ and Na^+ due to the lower solubility of the salts of the former cations. For the same reason, K^+ concentration has decreased in all magnetized biochars except BWS3 as most of it was removed during the water washing stage of magnetization. This is also evident from the low total K content (Table 5). The Na^+ concentration in magnetized biochar is from NaOH used during chemical co-precipitation. More washing with distilled water at the end of co-precipitation is recommended to reduce the sodium salt impurities in biochars after an ex-situ chemical magnetization. Mg^{2+} and Cl^- leaching is not influenced by magnetization. Among the magnetized variants, BWS3 has the most Ca^{2+} leaching, and overall Ca content. This type of water removability of alkali metals is also seen in ref (Kong et al. 2014).

The phosphate ions are water insoluble due to interaction with Fe and Ca (Rajapaksha et al. 2015) and the high pH of BWS0. These biochars are thus a slow-release P-source in the soil minimizing the eutrophication of freshwater sources. Owing to a lack of water-soluble nitrates and phosphates, in the short term, BWS0 might require complimentary amenders like compost. This has been seen in other biochars derived from lignin-rich precursors (Yang et al. 2015). However, it is worth noting that, nitrogen is not completely lost during pyrolysis. Some nitrogen is bound to the biochar matrix ("Elemental and Fiber Analysis" section) and can become bio-available with the aging of the biochar (Jamroz et al. 2020). Smaller dissolution concentrations of ammonium ions can support in reducing ammonification, and autotrophic nitrification rate, and alter soil urease activities; thereby lowering N_2O emissions. Alkaline pH increases water-soluble NH_4^+ concentration (Zhang et al. 2022). These ions can be adsorbed on biochar through electrostatic interactions with the negative functional groups (Heaney et al. 2018). The introduction of iron sulfate salts increases the SO_4^{2-} leaching from the magnetized biochars. By increasing the biochar loading rate in soil its ionic strength can be raised and promote flocculation that was adversely affected by zeta potential ζ (Bakshi et al. 2014). The low EC-value and the low concentrations of Na^+ and Cl^- and SO_4^{2-} facilitate BWS0 to be applicable in saline soil in arid regions at a higher loading rate (Yang et al. 2015).

About 0.4 to 0.9×10^{12} kg of terrestrial DOC annually flows into the oceans (Nebbioso and Piccolo 2013). It affects the biosphere through chelation and solubility of metals, transport of organic pollutants, alterations in microbial growth rate, photochemical reactions in water, and nutrient cycling. Hence, the biosphere is sensitive to the DOC incorporation from anthropogenic sources such as biochar. The DOC of pyrolysis-derived biochar decreases at higher HTTs and is usually lower than that from manure (Singh et al. 2017; Peng et al. 2020). Here, DOC from magnetized biochar is considerably larger than that from BWS0 (19.75 mg L^{-1}) owing to the larger cation concentration in the latter. The low negative electric charge of BWS2

(ζ = -18.34 mV) also facilitates the adsorption of negatively charged DOC but these ionic bonds are easily disassociated in water compared to those of polyvalent cations such as Ca^{2+} (Setia et al. 2013). Hence, BWS2 leaches the most DOC among the magnetic variants. The DOC from all WS biochar is the least aromatic ($SUVA_{254} < 2$ to 3 L mg^{-1} m^{-1}) (Wang et al. 2013; Zhang and He 2015) compared to humic acids (Ateia et al. 2017). A decrease in $SUVA_{254}$ after magnetization confirms that the additional DOC that is leached from them is hydrophilic and easily biodegradable aliphatic carbon. This also agrees with the E2/E3 ratio, which indicates that the biochar-derived DOC from magnetized biochar is predominantly carbon of low molecular weight. BWS0 can lower the export of low molecular and humified DOC due to microporosity and π-π interactions on its carbon surface, respectively (Shimabuku et al. 2016). However, this would also lead to fouling (Greiner et al. 2018) during adsorption applications whereby the adsorption of a target pollutant in natural waters is affected by the background DOC.

Potential environmental applications

Based on the investigated physico-chemical properties of WS-derived biochar, the following inferences may be drawn with respect to their applicability in environmental applications such as carbon sequestration, soil amelioration, and liquid-phase adsorption. BWS0 has a carbon sequestration potential of 0.84 kg CO_2/kg biomass. The carbon in BWS0 is 83% aromatic with a BC_{+100} of 98.23% and the PAH mainly consists of naphthalene, biphenyl, and phenanthrene, which are biodegradable. Magnetization tends to reduce the H/C_{org}, $O/C_{org,}$ and BC_{+100}, while increasing the oxidation stability.

The C/N of BWS0 is optimal for promoting microbial growth in soil. The loading rate of BWS0 should be high to counteract its dispersion in soil. It must also be mixed with N and P-rich compost or fertilizers. Heavy metal enrichment in biochar from WS is less compared to that from waste biomass from agricultural and industrial processes. The low DOC from unmagnetized biochar abates the risk of contaminant transport in soils (Sun et al. 2021) while their adsorption affinity toward DOC can reduce the eutrophication of aquatic reservoirs due to DOC leaching. These biochars poorly adsorb species like P oxy-anions and nitrates and may show relatively better adsorption capacity for cations like K^+ and NH_4^+. However, combined with the high porosity, the low ζ of BWS0 should improve the water holding capacity in most hydrophilic soils (Batista et al. 2018). BWS0 can lower the leaching of cationic plant nutrients and the alkalinity of acidic soils. It is beneficial to mix WS biochar with compost or other organic fertilizers since a) it is a slow-release source of N and P, b) has Cr above the LGV limit, and c) has higher colloidal stability. The π-π electron-donor interactions can improve its selectiveness for pollutants such as PAH in soils. Detailed correlation between biochar DOC characteristics and soil microbial community is still relatively unexplored in literature (Nobaharan et al. 2021) and must be investigated.

The WS biochar derived from the UCP_y in this investigation is not suitable for the adsorption of anionic adsorbates and can show preferential adsorption of DOC in aqueous solutions. Surface sorption of metal ions may be improved by washing and activating BWS0. This can remove impurities, create more oxygenated functional groups, and improve porosity. Adsorption of cationic contaminants such as As(V) or As(III) through electrostatic interaction is possible in a wide variety of solutions due to the low pH_{pzc} of BWS0. Compared to the magnetic WS biochar, BWS0 can show relatively good adsorption potential for hydrophobic contaminants and cations over a wide pH range, whereas the relatively acidic magnetic variants can show selectiveness for polar organic contaminants (Isaeva et al. 2021) and complex more with some metal ions due to relatively more OFGs.

Conclusion

Biochar was synthesized from walnut shells through UCPy in a garden oven. The generated biochar was magnetized through ex-situ chemical co-precipitation of iron salts. The applications of these biochars in carbon sequestration, soil amendment, and pollutant adsorption are greatly influenced by their properties. Hence, the physio-chemical properties of these biochars and the characteristics of water-extractable fractions from their carbon matrix were comprehensively investigated. Despite being produced from a lower-cost process without control over heating rate, HTT, and purge rate, WS biochars show promising properties to enable their intended environmental applications similar to those produced in the lab through CPy.

With the synthesized WS biochar, further investigations in the direction of soil incubation, and adsorption capacity for DOC are recommended. Synthesizing biochar in the laboratory has been mainly focused on highly organized and controlled conditions of production. More research into UCPy of biomass, as in the case of Terra preta, is required to reduce the cost of adoption of biochar as a product for environmental applications, especially in emerging economies.

Supplementary Information The online version contains supplementary material available at https://doi.org/10.1007/s10098-023-02525-z.

Acknowledgments The authors recognize the laboratory support provided by PD Dr. Stefan Dultz and Roger-Michael Klatt (retired) at the Institute of Soil Science, Leibniz University Hanover (LUH). Miss. Maren Prediger at the Institute of Micro Production Technology (IMPT), LUH. Benjamin Grüger at the Institute for Sanitary Engineering and Waste Management (ISAH), LUH. Prof. Alexander Marchanka, Institute of Organic Chemistry and Centre of Biomolecular Drug Research (OCI), LUH.

Author contributions Conceptualization and methodology were contributed by RRN, DW; experiments were contributed by RRN, AS, LK, AET, JL; data curation and visualization were contributed by RRN, AS; formal analysis was contributed by RRN; writing (original draft) was contributed by RRN; writing (review and editing) was contributed by RRN, AS, LK, AET, JL, MS, HE, JP, PB, DW; supervision was contributed by DW, PB, JP; funding and resources were contributed by DW, PB, JP, MS, HE; project administration was contributed by DW, PB, JP, MS, HE; all authors have read and agreed to the published version of the manuscript.

Funding Open Access funding enabled and organized by Projekt DEAL. PhD Fellowship German Academic Exchange Service (DAAD) Program number 57381412. P.B. acknowledges funding from the German Research Foundation (Deutsche Forschungsgemeinschaft—DFG) under project number 280642759.

Data availability Available upon request.

Declarations

Competing interests The authors declare no competing interests.

References

Ahmed MB, Zhou JL, Ngo HH, Guo W (2016) Insight into biochar properties and its cost analysis. Biomass Bioenerg 84:76–86. https://doi.org/10.1016/j.biombioe.2015.11.002

Aller D, Bakshi S, Laird DA (2017) Modified method for proximate analysis of biochars. J Anal Appl Pyrol 124:335–342. https://doi.org/10.1016/j.jaap.2017.01.012

Altun T, Pehlivan E (2012) Removal of Cr(VI) from aqueous solutions by modified walnut shells. Food Chem 132(2):693–700. https://doi.org/10.1016/j.foodchem.2011.10.099

Álvarez-Merino MA, Fontecha-Cámara MA, López-Ramón MV, Moreno-Castilla C (2008) Temperature dependence of the point of zero charge of oxidized and non-oxidized activated carbons. Carbon 46(5):778–787. https://doi.org/10.1016/j.carbon.2008.02.002

Amin FR, Huang Y, He Y, Zhang R, Liu G, Chen C (2016) Biochar applications and modern techniques for characterization. Clean Technol Environ Policy 18(5):1457–1473. https://doi.org/10.1007/s10098-016-1218-8

Ateia M, Apul OG, Shimizu Y, Muflihah A, Yoshimura C, Karanfil T (2017) Elucidating adsorptive fractions of natural organic matter on carbon nanotubes. Environ Sci Technol 51(12):7101–7110. https://doi.org/10.1021/acs.est.7b01279

Bakshi S, He ZL, Harris WG (2014) Biochar amendment affects leaching potential of copper and nutrient release behavior in contaminated sandy soils. J Environ Qual 43(6):1894–1902. https://doi.org/10.2134/jeq2014.05.0213

Batista E, Shultz J, Matos TTS, Fornari MR, Ferreira TM, Szpoganicz B, de Freitas RA, Mangrich AS (2018) Effect of surface and porosity of biochar on water holding capacity aiming indirectly at preservation of the Amazon biome. Sci Rep 8(1):10677. https://doi.org/10.1038/s41598-018-28794-z

Brust GE (2019) Management strategies for organic vegetable fertility. In: Safety and Practice for Organic Food. pp 193–212. doi:https://doi.org/10.1016/b978-0-12-812060-6.00009-x

Budai A, Zimmerman AR, Cowie AL, Webber JBW, Singh JP, Glaser B, Masiello CA et al. (2013) Biochar carbon stability test method: an assessment of methods to determine biochar carbon stability. Int Biochar Initiative,

Carrier M, Hardie AG, Uras Ü, Görgens J, Knoetze J (2012) Production of char from vacuum pyrolysis of South-African sugar cane bagasse and its characterization as activated carbon and biochar. J Anal Appl Pyrol 96:24–32. https://doi.org/10.1016/j.jaap.2012.02.016

Cayuela ML, Jeffery S, van Zwieten L (2015) The molar H: Corg ratio of biochar is a key factor in mitigating N2O emissions from soil. Agr Ecosyst Environ 202:135–138. https://doi.org/10.1016/j.agee.2014.12.015

Cazetta AL, Pezoti O, Bedin KC, Silva TL, Paesano Junior A, Asefa T, Almeida VC (2016) Magnetic activated carbon derived from biomass waste by concurrent synthesis: efficient adsorbent for toxic dyes. ACS Sustain Chem Eng 4(3):1058–1068. https://doi.org/10.1021/acssuschemeng.5b01141

CBI (2019) Exporting walnuts to Europe. Ministry of Foreign Affairs. https://www.cbi.eu/market-information/processed-fruit-vegetables-edible-nuts/walnuts. Accessed 19 May 2022

Ch'ng HY, Haruna AO, Majid NMNA, Jalloh MB (2019) Improving soil phosphorus availability and yield of Zea mays l. using biochar and compost derived from agro-industrial wastes. Ital J Agron 14(1):34–42. https://doi.org/10.4081/ija.2019.1107

Channiwala SA, Parikh PP (2002) A unified correlation for estimating HHV of solid, liquid and gaseous fuels. Fuel 81(8):1051–1063. https://doi.org/10.1016/s0016-2361(01)00131-4

Childres I, Jauregui LA, Park W, Cao H, Chen YP (2013) Raman spectroscopy of graphene and related materials. New Dev Photon Mater Res 1:1–20

Dickinson D, Balduccio L, Buysse J, Ronsse F, van Huylenbroeck G, Prins W (2015) Cost-benefit analysis of using biochar to improve cereals agriculture. GCB Bioenergy 7(4):850–864. https://doi.org/10.1111/gcbb.12180

Duan X, Zhang C, Srinivasakannan C, Wang X (2017) Waste walnut shell valorization to iron loaded biochar and its application to arsenic removal. Resour Effic Technol 3(1):29–36. https://doi.org/10.1016/j.reffit.2017.01.001

EBC (2012) European Biochar Certificate - Guidelines for a Sustainable Production of Biochar. European Biochar Foundation (EBC). Arbaz, Switzerland

Fan Q, Cui L, Quan G, Wang S, Sun J, Han X, Wang J, Yan J (2018) Effects of wet oxidation process on biochar surface in acid and alkaline soil environments. Materials. https://doi.org/10.3390/ma11122362

Garcia R, Pizarro C, Lavin AG, Bueno JL (2013) Biomass proximate analysis using thermogravimetry. Bioresour Technol 139:1–4. https://doi.org/10.1016/j.biortech.2013.03.197

Glaser B, Birk JJ (2012) State of the scientific knowledge on properties and genesis of Anthropogenic Dark Earths in Central Amazonia (terra preta de Índio). Geochim Cosmochim Acta 82:39–51. https://doi.org/10.1016/j.gca.2010.11.029

Golubev YA, Rozhkova NN, Kabachkov EN, Shul'ga YM, Natkaniec-Hołderna K, Natkaniec I, Antonets IV, Makeev BA, Popova NA, Popova VA, Sheka EF (2019) sp amorphous

carbons in view of multianalytical consideration: normal, expected and new. J Non-Cryst Solids. https://doi.org/10.1016/j.jnoncrysol.2019.119608

Greiner BG, Shimabuku KK, Summers RS (2018) Influence of biochar thermal regeneration on sulfamethoxazole and dissolved organic matter adsorption. Environ Sci Water Res Technol 4(2):169–174. https://doi.org/10.1039/c7ew00379j

Guo K, Zhao Y, Liu Y, Chen J, Wu Q, Ruan Y, Li S, Shi J, Zhao L, Sun X, Liang C, Xu Q, Qin H (2020) Pyrolysis temperature of biochar affects ecoenzymatic stoichiometry and microbial nutrient-use efficiency in a bamboo forest soil. Geoderma. https://doi.org/10.1016/j.geoderma.2019.114162

Gupta S, Gupta GK, Mondal MK (2019) Slow pyrolysis of chemically treated walnut shell for valuable products: effect of process parameters and in-depth product analysis. Energy 181:665–676. https://doi.org/10.1016/j.energy.2019.05.214

He X, Jiang J, Hong Z, Pan X, Dong Y, Xu R (2020) Effect of aluminum modification of rice straw–based biochar on arsenate adsorption. J Soils Sediments 20(8):3073–3082. https://doi.org/10.1007/s11368-020-02595-2

Heaney N, Mamman M, Tahir H, Al-Gharib A, Lin C (2018) Effects of softwood biochar on the status of nitrogen species and elements of potential toxicity in soils. Ecotoxicol Environ Saf 166:383–389. https://doi.org/10.1016/j.ecoenv.2018.09.112

Hong M, Zhang L, Tan Z, Huang Q (2019) Effect mechanism of biochar's zeta potential on farmland soil's cadmium immobilization. Environ Sci Pollut Res Int 26(19):19738–19748. https://doi.org/10.1007/s11356-019-05298-5

Hussain SZ, Ammatullah B, Kanojia V, Reshi M, Naseer B, Naik HR (2018) Design and development of technology for walnut cracking. J Food Sci Technol 55(12):4973–4983. https://doi.org/10.1007/s13197-018-3435-0

Igalavithana AD, Mandal S, Niazi NK, Vithanage M, Parikh SJ, Mukome FND, Rizwan M, Oleszczuk P, Al-Wabel M, Bolan N, Tsang DCW, Kim K-H, Ok YS (2018) Advances and future directions of biochar characterization methods and applications. Crit Rev Environ Sci Technol 47(23):2275–2330. https://doi.org/10.1080/10643389.2017.1421844

Isaeva VI, Vedenyapina MD, Kurmysheva AY, Weichgrebe D, Nair RR, Nguyen NPT, Kustov LM (2021) Modern carbon-based materials for adsorptive removal of organic and inorganic pollutants from water and wastewater. Molecules. https://doi.org/10.3390/molecules26216628

Jack J, Huggins TM, Huang Y, Fang Y, Ren ZJ (2019) Production of magnetic biochar from waste-derived fungal biomass for phosphorus removal and recovery. J Clean Prod 224:100–106. https://doi.org/10.1016/j.jclepro.2019.03.120

Jamroz E, Bekier J, Medynska-Juraszek A, Kaluza-Haladyn A, Cwielag-Piasecka I, Bednik M (2020) The contribution of water extractable forms of plant nutrients to evaluate MSW compost maturity: a case study. Sci Rep 10(1):12842. https://doi.org/10.1038/s41598-020-69860-9

Jaramillo J, Álvarez PM, Gómez-Serrano V (2010) Oxidation of activated carbon by dry and wet methods. Fuel Process Technol 91(11):1768–1775. https://doi.org/10.1016/j.fuproc.2010.07.018

Kambarova GB, Sarymsakov S (2008) Preparation of activated charcoal from walnut shells. Solid Fuel Chem 42(3):183–186. https://doi.org/10.3103/s0361521908030129

Karim AA, Kumar M, Mohapatra S, Singh SK, Panda CR (2018) Coplasma processing of banana peduncle with phosphogypsum waste for production of lesser toxic potassium–sulfur rich biochar. J Mater Cycles Waste Manage 21(1):107–115. https://doi.org/10.1007/s10163-018-0769-7

Kaya N, Arslan F, Yildiz Uzun Z (2020) Production and characterization of carbon-based adsorbents from waste lignocellulosic biomass: their effectiveness in heavy metal removal. Fuller Nanotub Carbon Nanostruct 28(10):769–780. https://doi.org/10.1080/1536383x.2020.1759556

Kong Z, Liaw SB, Gao X, Yu Y, Wu H (2014) Leaching characteristics of inherent inorganic nutrients in biochars from the slow and fast pyrolysis of mallee biomass. Fuel 128:433–441. https://doi.org/10.1016/j.fuel.2014.03.025

Lahijani P, Mohammadi M, Mohamed AR (2018) Metal incorporated biochar as a potential adsorbent for high capacity CO_2 capture at ambient condition. J CO2 Util 26:281–293. https://doi.org/10.1016/j.jcou.2018.05.018

Leng L, Huang H, Li H, Li J, Zhou W (2019) Biochar stability assessment methods: a review. Sci Total Environ 647:210–222. https://doi.org/10.1016/j.scitotenv.2018.07.402

Leng L, Xiong Q, Yang L, Li H, Zhou Y, Zhang W, Jiang S, Li H, Huang H (2021) An overview on engineering the surface area and porosity of biochar. Sci Total Environ 763:144204. https://doi.org/10.1016/j.scitotenv.2020.144204

Li P, Hur J (2017) Utilization of UV-Vis spectroscopy and related data analyses for dissolved organic matter (DOM) studies: a review. Crit Rev Environ Sci Technol 47(3):131–154. https://doi.org/10.1080/10643389.2017.1309186

Li X, Wang C, Zhang J, Liu J, Liu B, Chen G (2020a) Preparation and application of magnetic biochar in water treatment: a critical review. Sci Total Environ 711:134847. https://doi.org/10.1016/j.scitotenv.2019.134847

Li Z, Hanafy H, Zhang L, Sellaoui L, Schadeck Netto M, Oliveira MLS, Seliem MK, Luiz Dotto G, Bonilla-Petriciolet A, Li Q (2020b) Adsorption of congo red and methylene blue dyes on an ashitaba waste and a walnut shell-based activated carbon from aqueous solutions: Experiments, characterization and physical interpretations. Chem Eng J 388:124263. https://doi.org/10.1016/j.cej.2020.124263

Liu T, Liu B, Zhang W (2015) Nutrients and heavy metals in biochar produced by sewage sludge pyrolysis: its application in soil amendment. Pol J Environ Stud 23(1):271–275

Long L, Xue Y, Hu X, Zhu Y (2019) Study on the influence of surface potential on the nitrate adsorption capacity of metal modified biochar. Environ Sci Pollut Res Int 26(3):3065–3074. https://doi.org/10.1007/s11356-018-3815-z

Mao J, Zhang K, Chen B (2019) Linking hydrophobicity of biochar to the water repellency and water holding capacity of biochar-amended soil. Environ Pollut 253:779–789. https://doi.org/10.1016/j.envpol.2019.07.051

Matthews MJ, Pimenta MA, Dresselhaus G, Dresselhaus MS, Endo M (1999) Origin of dispersive effects of the RamanDband in carbon materials. Phys Rev B 59(10):R6585–R6588. https://doi.org/10.1103/PhysRevB.59.R6585

Maziarka P, Wurzer C, Arauzo PJ, Dieguez-Alonso A, Mašek O, Ronsse F (2021) Do you BET on routine? The reliability of N2 physisorption for the quantitative assessment of biochar's surface area. Chem Eng J. https://doi.org/10.1016/j.cej.2021.129234

Nair RR, Mondal MM, Weichgrebe D (2020) Biochar from co-pyrolysis of urban organic wastes—investigation of carbon sink potential using ATR-FTIR and TGA. Biomass Convers Biorefinery. https://doi.org/10.1007/s13399-020-01000-9

Nebbioso A, Piccolo A (2013) Molecular characterization of dissolved organic matter (DOM): a critical review. Anal Bioanal Chem 405(1):109–124. https://doi.org/10.1007/s00216-012-6363-2

Nguyen TX, Bhatia SK (2009) Accessibility of simple gases in disordered carbons: theory and simulation. Asia-Pac J Chem Eng 4(5):557–562. https://doi.org/10.1002/apj.282

Nobaharan K, Bagheri Novair S, Asgari Lajayer B, van Hullebusch E (2021) Phosphorus removal from wastewater: the potential use of biochar and the key controlling factors. Water. https://doi.org/10.3390/w13040517

Parikh J, Channiwala S, Ghosal G (2005) A correlation for calculating HHV from proximate analysis of solid fuels. Fuel 84(5):487–494. https://doi.org/10.1016/j.fuel.2004.10.010

Peng N, Wang K, Tu N, Liu Y, Li Z (2020) Fluorescence regional integration combined with parallel factor analysis to quantify fluorescencent spectra for dissolved organic matter released from manure biochars. RSC Adv 10(52):31502–31510. https://doi.org/10.1039/d0ra02706e

Pérez E, Sulbarán M, Ball MM, Yarzábal LA (2007) Isolation and characterization of mineral phosphate-solubilizing bacteria naturally colonizing a limonitic crust in the south-eastern Venezuelan region. Soil Biol Biochem 39(11):2905–2914. https://doi.org/10.1016/j.soilbio.2007.06.017

Pirayesh H, Khazaeian A, Tabarsa T (2012) The potential for using walnut (Juglans regia L.) shell as a raw material for wood-based particleboard manufacturing. Compos Part B Eng 43(8):3276–3280. https://doi.org/10.1016/j.compositesb.2012.02.016

Qin Y, Wang C, Sun X, Ma Y, Song X, Wang F, Li K, Ning P (2021) Defects on activated carbon determine the dispersion of active components and thus the simultaneous removal efficiency of SO2, NOx and Hg0. Fuel. https://doi.org/10.1016/j.fuel.2021.120391

Qiu Z, Chen J, Tang J, Zhang Q (2018) A study of cadmium remediation and mechanisms: Improvements in the stability of walnut shell-derived biochar. Sci Total Environ 636:80–84. https://doi.org/10.1016/j.scitotenv.2018.04.215

Rajapaksha AU, Ahmad M, Vithanage M, Kim KR, Chang JY, Lee SS, Ok YS (2015) The role of biochar, natural iron oxides, and nanomaterials as soil amendments for immobilizing metals in shooting range soil. Environ Geochem Health 37(6):931–942. https://doi.org/10.1007/s10653-015-9694-z

Rombolà AG, Fabbri D, Meredith W, Snape CE, Dieguez-Alonso A (2016) Molecular characterization of the thermally labile fraction of biochar by hydropyrolysis and pyrolysis-GC/MS. J Anal Appl Pyrol 121:230–239. https://doi.org/10.1016/j.jaap.2016.08.003

Russo C, Stanzione F, Tregrossi A, Ciajolo A (2014) Infrared spectroscopy of some carbon-based materials relevant in combustion: Qualitative and quantitative analysis of hydrogen. Carbon 74:127–138. https://doi.org/10.1016/j.carbon.2014.03.014

Sahin O, Taskin MB, Kaya EC, Atakol O, Emir E, Inal A, Gunes A, Nicholson F (2017) Effect of acid modification of biochar on nutrient availability and maize growth in a calcareous soil. Soil Use Manag 33(3):447–456. https://doi.org/10.1111/sum.12360

Senol H (2021) Effects of NaOH, thermal, and combined NaOH-thermal pretreatments on the biomethane yields from the anaerobic digestion of walnut shells. Environ Sci Pollut Res Int 28(17):21661–21673. https://doi.org/10.1007/s11356-020-11984-6

Setia R, Rengasamy P, Marschner P (2013) Effect of mono- and divalent cations on sorption of water-extractable organic carbon and microbial activity. Biol Fertil Soils 50(5):727–734. https://doi.org/10.1007/s00374-013-0888-1

Shah MA, Khan MNS, Kumar V (2018) Biomass residue characterization for their potential application as biofuels. J Therm Anal Calorim 134(3):2137–2145. https://doi.org/10.1007/s10973-018-7560-9

Shimabuku KK, Kearns JP, Martinez JE, Mahoney RB, Moreno-Vasquez L, Summers RS (2016) Biochar sorbents for sulfamethoxazole removal from surface water, stormwater, and wastewater effluent. Water Res 96:236–245. https://doi.org/10.1016/j.watres.2016.03.049

Sieng-Huat K (2019) Palm kernel shell biochar production, characteristics and carbon sequestration potential. J Oil Palm Res. https://doi.org/10.21894/jopr.2019.0041

Singh B, Camps-Arbestain M, Johannes L (2017) Biochar a guide to analytical methods. CRC Press/Taylor and Francis Group, LLC

Spokas KA, Novak JM, Masiello CA, Johnson MG, Colosky EC, Ippolito JA, Trigo C (2014) Physical disintegration of biochar: an overlooked process. Environ Sci Technol Lett 1(8):326–332. https://doi.org/10.1021/ez500199t

Suliman W, Harsh JB, Abu-Lail NI, Fortuna AM, Dallmeyer I, Garcia-Perez M (2017) The role of biochar porosity and surface functionality in augmenting hydrologic properties of a sandy soil. Sci Total Environ 574:139–147. https://doi.org/10.1016/j.scitotenv.2016.09.025

Sun Y, Xiong X, He M, Xu Z, Hou D, Zhang W, Ok YS, Rinklebe J, Wang L, Tsang DCW (2021) Roles of biochar-derived dissolved organic matter in soil amendment and environmental remediation: a critical review. Chem Eng J. https://doi.org/10.1016/j.cej.2021.130387

Tate RL (2020) Soil microbiology. 3rd edn, John Wiley & Sons Inc.

Thines KR, Abdullah EC, Mubarak NM, Ruthiraan M (2017) Synthesis of magnetic biochar from agricultural waste biomass to enhancing route for waste water and polymer application: a review. Renew Sustain Energy Rev 67:257–276. https://doi.org/10.1016/j.rser.2016.09.057

Thommes M, Kaneko K, Neimark AV, Olivier JP, Rodriguez-Reinoso F, Rouquerol J, Sing KSW (2015) Physisorption of gases, with special reference to the evaluation of surface area and pore size distribution (IUPAC Technical Report). Pure Appl Chem 87(9–10):1051–1069. https://doi.org/10.1515/pac-2014-1117

Toth G, Hermann T, Da Silva MR, Montanarella L (2016) Heavy metals in agricultural soils of the European Union with implications for food safety. Environ Int 88:299–309. https://doi.org/10.1016/j.envint.2015.12.017

USDA (2022) Tree Nuts: World Markets and Trade (trans: Service FA). United States Department of Agriculture,

Uslu OS, Babur E, Alma MH, Solaiman ZM (2020) Walnut shell biochar increases seed germination and early growth of seedlings of fodder crops. Agriculture. https://doi.org/10.3390/agriculture10100427

Verma L, Singh J (2019) Synthesis of novel biochar from waste plant litter biomass for the removal of Arsenic (III and V) from aqueous solution: a mechanism characterization, kinetics and thermodynamics. J Environ Manage 248:109235. https://doi.org/10.1016/j.jenvman.2019.07.006

Volkov D, Rogova O, Proskurnin M (2021) Temperature dependences of IR spectra of humic substances of brown coal. Agronomy. https://doi.org/10.3390/agronomy11091822

Wan X, Li C, Parikh SJ (2020) Simultaneous removal of arsenic, cadmium, and lead from soil by iron-modified magnetic biochar. Environ Pollut 261:114157. https://doi.org/10.1016/j.envpol.2020.114157

Wan J, Liu F, Wang G, Liang W, Peng C, Zhang W, Lin K, Yang J (2021) Exploring different mechanisms of biochars in removing hexavalent chromium: sorption, reduction and electron shuttle. Bioresour Technol 337:125382. https://doi.org/10.1016/j.biortech.2021.125382

Wang L, Zhao J, Sun YY, Zhang SB (2011) Characteristics of Raman spectra for graphene oxide from ab initio simulations. J Chem Phys 135(18):184503. https://doi.org/10.1063/1.3658859

Wang Y, Zhang D, Shen Z, Feng C, Chen J (2013) Revealing sources and distribution changes of dissolved organic matter (DOM) in pore water of sediment from the Yangtze estuary. PLoS ONE 8(10):e76633. https://doi.org/10.1371/journal.pone.0076633

Wang SY, Tang YK, Li K, Mo YY, Li HF, Gu ZQ (2014) Combined performance of biochar sorption and magnetic separation processes for treatment of chromium-contained electroplating wastewater. Bioresour Technol 174:67–73. https://doi.org/10.1016/j.biortech.2014.10.007

Wang J, Liu M, Wu H, Peng J, Peng B, Yang Y, Cao M, Wei H, Xie H (2022) Design and key parameter optimization of conic roller

shelling device based on walnut moisture-regulating treatments. Agriculture. https://doi.org/10.3390/agriculture12040561
Woods WI, Teixeira WG, Lehmann J, Steiner C, WinklerPrins A, Rebellato L (2009) Amazonian dark earths: wim Sombroek's vision. doi:https://doi.org/10.1007/978-1-4020-9031-8
Wu W, Yang M, Feng Q, McGrouther K, Wang H, Lu H, Chen Y (2012) Chemical characterization of rice straw-derived biochar for soil amendment. Biomass Bioenerg 47:268–276. https://doi.org/10.1016/j.biombioe.2012.09.034
Wurzer C, Masek O (2021) Feedstock doping using iron rich waste increases the pyrolysis gas yield and adsorption performance of magnetic biochar for emerging contaminants. Bioresour Technol 321:124473. https://doi.org/10.1016/j.biortech.2020.124473
Xiao X, Chen Z, Chen B (2016) H/C atomic ratio as a smart linkage between pyrolytic temperatures, aromatic clusters and sorption properties of biochars derived from diverse precursory materials. Sci Rep 6:22644. https://doi.org/10.1038/srep22644
Xu G, Zhang Y, Shao H, Sun J (2016) Pyrolysis temperature affects phosphorus transformation in biochar: chemical fractionation and (31)P NMR analysis. Sci Total Environ 569–570:65–72. https://doi.org/10.1016/j.scitotenv.2016.06.081
Xu CY, Li QR, Geng ZC, Hu FN, Zhao SW (2020) Surface properties and suspension stability of low-temperature pyrolyzed biochar nanoparticles: effects of solution chemistry and feedstock sources. Chemosphere 259:127510. https://doi.org/10.1016/j.chemosphere.2020.127510
Yang F, Lee X-q, Wang B (2015) Characterization of biochars produced from seven biomasses grown in three different climate zones. Chin J Geochem 34(4):592–600. https://doi.org/10.1007/s11631-015-0072-4
Yang X, Jin D, Zhang M, Wu P, Jin H, Li J, Wang X, Ge H, Wang Z, Lou H (2016) Fabrication and application of magnetic starch-based activated hierarchical porous carbon spheres for the efficient removal of dyes from water. Mater Chem Phys 174:179–186. https://doi.org/10.1016/j.matchemphys.2016.02.073
Yi Y, Huang Z, Lu B, Xian J, Tsang EP, Cheng W, Fang J, Fang Z (2020) Magnetic biochar for environmental remediation: a review. Bioresour Technol 298:122468. https://doi.org/10.1016/j.biortech.2019.122468
Yin Y, Yin J, Zhang W, Tian H, Hu Z, Ruan M, Song Z, Liu L (2018) Effect of char structure evolution during pyrolysis on combustion characteristics and kinetics of waste biomass. J Energy Resour Technol. https://doi.org/10.1115/1.4039445
Yuan T, He W, Yin G, Xu S (2020) Comparison of bio-chars formation derived from fast and slow pyrolysis of walnut shell. Fuel. https://doi.org/10.1016/j.fuel.2019.116450
Zhang J, Lü F, Luo C, Shao L, He P (2014) Humification characterization of biochar and its potential as a composting amendment. J Environ Sci 26(2):390–397. https://doi.org/10.1016/s1001-0742(13)60421-0
Zhang P, Huang P, Xu X, Sun H, Jiang B, Liao Y (2020a) Spectroscopic and molecular characterization of biochar-derived dissolved organic matter and the associations with soil microbial responses. Sci Total Environ 708:134619. https://doi.org/10.1016/j.scitotenv.2019.134619
Zhang P, Shao Y, Xu X, Huang P, Sun H (2020b) Phototransformation of biochar-derived dissolved organic matter and the effects on photodegradation of imidacloprid in aqueous solution under ultraviolet light. Sci Total Environ 724:137913. https://doi.org/10.1016/j.scitotenv.2020.137913
Zhang J, Zhang X, Sun H, Wang C, Zhou S (2022) Carbon sequestration and nutrients improvement meditated by biochar in a 3-year vegetable rotation system. J Soils Sediments 22(5):1385–1396. https://doi.org/10.1007/s11368-022-03175-2
Zhang M, He Z (2015) Characteristics of dissolved organic carbon revealed by ultraviolet-visible absorbance and fluorescence spectroscopy: The current status and future exploration. In: labile organic matter-chemical compositions, function, and significance in soil and the environment. SSSA Special Publications. pp 1–21. doi:https://doi.org/10.2136/sssaspecpub62.2014.0032
Zhao L, Cao X, Masek O, Zimmerman A (2013) Heterogeneity of biochar properties as a function of feedstock sources and production temperatures. J Hazard Mater 256–257:1–9. https://doi.org/10.1016/j.jhazmat.2013.04.015
Zhao L, Cao X, Zheng W, Wang Q, Yang F (2015) Endogenous minerals have influences on surface electrochemistry and ion exchange properties of biochar. Chemosphere 136:133–139. https://doi.org/10.1016/j.chemosphere.2015.04.053
Zhao Z, Wu Q, Nie T, Zhou W (2019) Quantitative evaluation of relationships between adsorption and partition of atrazine in biochar-amended soils with biochar characteristics. RSC Adv 9(8):4162–4171. https://doi.org/10.1039/c8ra08544g
Zuo L, Lin R, Shi Q, Xu S (2020) Evaluation of the bioavailability of heavy metals and phosphorus in biochar derived from manure and manure digestate. Water Air Soil Pollut. https://doi.org/10.1007/s11270-020-04924-0